

Methods for the Detection of the Epoch of Reionization
by Interferometers Measuring the 21 cm Signal

By

Carina Cheng

A dissertation submitted in partial satisfaction of the

requirements for the degree of

Doctor of Philosophy

in

Astrophysics

in the

Graduate Division

of the

University of California, Berkeley

Committee in charge:

Professor Aaron Parsons, Chair

Professor Stuart Bale

Professor Mariska Kriek

Spring 2019

Methods for the Detection of the Epoch of Reionization
by Interferometers Measuring the 21 cm Signal

Copyright 2019
by
Carina Cheng

Abstract

Methods for the Detection of the Epoch of Reionization by Interferometers Measuring the 21 cm Signal

by

Carina Cheng

Doctor of Philosophy in Astrophysics

University of California, Berkeley

Professor Aaron Parsons, Chair

The Epoch of Reionization is one of the last unexplored eras of our Universe's history. Beginning about a billion years after the Big Bang, this epoch is characterized by the births of the first stars and galaxies, whose light subsequently altered the nature of the gas surrounding them. There are several experiments aiming to detect the phase transition of this gas as it changes from neutral hydrogen to ionized hydrogen. Such a detection would open a wealth of information about our early Universe, revealing details about the nature of the first luminous sources and the evolution of structure formation.

Interferometers such as the Precision Array for Probing the Epoch of Reionization (PAPER) and the Hydrogen Epoch of Reionization Array (HERA) seek to measure the 21 cm signal from neutral hydrogen and map its evolution over spatial and temporal scales. A successful detection of reionization, however, is a difficult measurement. Though the 21 cm signal is a powerful topological probe of the intergalactic medium, it is easily buried underneath bright foreground signals and instrumental systematics. A clean detection of reionization is ambitious and requires analysis methods that maximize data sensitivity and increase confidence in results.

The work presented in this thesis addresses many of the key challenges that face the current field of 21 cm cosmology. This includes algorithms to locate contaminated data, methods to ensure accurate power spectrum measurements, and techniques for removing unwanted systematics while preserving the reionization signal. These developments serve as the foundation of the latest 21 cm measurements from the PAPER-64 and PAPER-128 arrays, whose results lie at the forefront of the field. These methods are also fundamental to HERA and future experiments, as they provide a strong foundation for the continued exploration of our cosmic dawn.

to my parents

Contents

List of Figures	iv
List of Tables	vii
Acknowledgments	viii
1 Introduction	1
1.1 The Epoch of Reionization	1
1.1.1 Cosmic History	1
1.1.2 CMB and Galaxy Measurements	2
1.1.3 Measurements of HI	4
1.1.4 This Thesis	8
1.2 Interferometry	8
1.2.1 The Visibility Equation	8
1.2.2 The 21 cm Power Spectrum	9
1.2.3 Calibration	10
1.2.4 Foreground Filtering	12
1.2.5 Fringe-rate Filtering	14
1.3 Instruments	14
1.3.1 The Precision Array for Probing the Epoch of Reionization	15
1.3.2 The Hydrogen Epoch of Reionization Array	17
1.3.3 Other Experiments and Status of Field	19
2 Power Spectrum Methods	22
2.1 Introduction to Themes	22
2.2 Signal Loss Toy Model	22
2.3 Signal Loss Mathematical Framework	22
2.4 Error Estimation Toy Model	22
2.5 Bias Toy Model	22
3 PAPER-64	23
3.1 Overview	23
3.1.1 Observations	23

3.1.2	Data Processing	24
3.1.3	Case Study Data	25
3.2	Signal Loss	26
3.3	Error Estimation	26
3.4	Bias	26
3.5	Power Spectrum Limits	26
4	PAPER-128	28
4.1	Overview	28
4.2	Quality Assurance	29
4.2.1	Flagging Julian Dates	30
4.2.2	Flagging Antennas	32
4.3	Data Processing	35
4.4	Power Spectrum Limits	37
5	HERA	39
6	Conclusion	40
Bibliography		41

List of Figures

1.1	Timeline of the history of the Universe. The Epoch of Reionization marks the era when the first stars and galaxies formed and ionized the neutral hydrogen in the Universe. Image credit: NAOJ.	2
1.2	A cartoon diagram of the observable Universe, centered on us. Close-by, galaxy observations have mapped out cosmic web structure in our nearby Universe (image credit: SDSS). Far-away, the cosmic microwave background is observed at a redshift of $z \sim 1100$ (image credit: WMAP). The Epoch of Reionization represents a largely unexplored era between the two, and can be probed by measuring red-shifted 21 cm radiation from neutral hydrogen.	5
1.3	The evolution of the global 21 cm signal, starting with the Dark Ages, through galaxy formation and reionization (image credit: Pritchard & Loeb (2012)). The work in this thesis mainly focuses on a redshift range of $6 < z < 12$ when reionization is expected to progress and complete.	6
1.4	The theoretical evolution of the cross-21 cm power spectrum for a specific model (image credit: Barkana (2009)), where the neutral fraction $x_{HI} = 10\%, 30\%, 50\%, 70\%, 90\%$, and 98% from top to bottom at large k . This figure shows the expected evolution of the power spectrum which interferometers seek to measure.	11
1.5	A cartoon diagram of the “EoR Window” and “wedge” of foreground contamination in Fourier space (image credit: Dillon et al. (2015b)). A foreground avoidance approach makes power spectrum measurements in the window, while a foreground subtraction approach subtracts out foregrounds so that measurements can be made in the wedge. The overall power spectrum measurement space is limited by an interferometer’s field of view and angular resolution along the horizontal axis, and spectral resolution and intrinsic foregrounds along the vertical axis.	13
1.6	A PAPER antenna in the Karoo Desert in South Africa. A dual-polarization dipole sits at the center, surrounded by wire mesh panels that measure 2 m on each side.	16

1.7 A HERA dish in the Karoo Desert in South Africa. Wire-mesh, PVC pipes, and wooden structures serve as the foundation for the 14 m diameter parabola. A PA-PER dipole is suspended upside-down with a wire pulley-system and surrounded by a prototype wire-mesh skirt structure. HERA-350 will use an updated design for its feed; however, HERA's initial data releases use the old PAPER infrastructure as depicted here.	18
1.8 The full HERA-350 array (image credit: DeBoer et al. (2017)). The array is comprised of a segmented densely-packed core (to optimize redundancy for a foreground avoidance approach) and surrounding outrigger elements (for imaging capabilities).	18
1.9 Published upper limits on the EoR placed by different 21 cm experiments, prior to the work in this thesis. All PAPER results shown (PAPER-32 is in cyan and magenta, and PAPER-64 is in blue) are suspect to the errors discussed throughout this work and are superseded by the ones presented in Chapter 3.	20
3.1 The PAPER-64 antenna layout. We use only 10 of the 30 m East/West baselines for the analysis in this paper (i.e., a subset of the shortest horizontal spacings).	24
3.2 Top: the normalized optimal power-spectrum sensitivity weighting in fringe-rate space for our fiducial baseline and Stokes I polarization beam. Bottom: the time domain convolution kernel corresponding to the top panel. Real and imaginary components are illustrated in cyan and magenta, respectively, with the absolute amplitude in black. The fringe-rate filter acts as an integration in time, increasing sensitivity but reducing the number of independent samples in the dataset.	27
4.1 The PAPER-128 antenna layout. There are 112 antennas arranged in a grid layout which are used for power spectrum analyses. The addition of 16 outrigger antennas is used to increase <i>uv</i> -plane sampling for imaging analyses.	29
4.2 Visibility amplitudes as a function of LST for different Julian days of data. The left column shows the data before (top) and after (bottom) the flagging of outlier days for Epoch 1. The right column shows similar data for Epoch 2.	31
4.3 Waterfall plots of visibility amplitudes for a “good” reference day (left) in Epoch 2 and “bad” day (right). We exclude corrupted data for specific days found with our metric.	32
4.4 Waterfall plots of visibility amplitudes for four different polarizations and two different baselines. Antenna 26 is found to be cross-polarized because its feed was rotated by 90 degrees, and hence its “X” and “Y” polarization states are mis-labeled. Equation (4.2) captures visibility amplitudes like the ones shown here in order to automatically detect cross-polarized antennae.	33

4.5	Flagged antennas, found using Equation (4.1), are marked in black for each antenna number (x-axis) and Julian date (y-axis). The left column shows flags for XX polarization, and the right column shows flags for YY polarization. The top row shows flags for Epoch 1 and the bottom row shows flags for Epoch 2. We remove antennas that are flagged greater than 50% of the time per epoch.	34
4.6	FirstCal phase solutions for Antenna 1 (Epoch 1, XX polarization) where no antennas are flagged (top left) and some antennas are flagged (via the methods described in Chapter 4.2.2, top right). Omnical χ^2 results are also shown for the two cases (bottom). We do not include any of the dead 16 antennas associated with correlator FX2. It is crucial to flag misbehaving antennas (especially extreme outlier antennas) prior to redundant calibration, motivating the development of automated quality assessment tools prior to the post-processing of data.	36
4.7	Power spectrum results for PAPER-128 season 1 data for two redshifts (rows) and two epochs (columns), using one baseline separation-type only (30 m East/West baselines). Black and gray points represent positive and negative power spectrum values, respectively, with 2σ error bars determined from bootstrapping. The 2σ theoretical noise sensitivity prediction is shown in green. Gray shaded regions correspond to theoretical errors on each data point.	38

List of Tables

4.1 An overview of the PAPER-128 data used for power spectrum analysis in this thesis.	30
--	----

Acknowledgments

This thesis may be filled with new scientific methods, exciting astronomical insights, and technical jargon. But what it doesn't capture, is what I'm most proud of — the life lessons I've learned about what it means to be a scientist, what it means to do good science, and how to learn and preservere despite challenges. For that, I must thank many people.

Chapter 1

Introduction

1.1 The Epoch of Reionization

Our Universe has a complex, rich history, of which enormous progress has been made in the past few decades to unravel its story. Much has been learned about the very beginnings of the Universe, from the Big Bang's large explosion of energy to the relatively smooth and simple cosmic background radiation that was leftover. Additionally, observational feats have revealed the status of the present-day Universe and the intricate *cosmic web*, or large scale structure, of galaxies today.

The Epoch of Reionization (EoR) ties these two bookends together, occurring about a billion years after the Big Bang when the very first stars and galaxies formed. How did the tiny density fluctuations from the cosmic microwave background develop into the structure we see today? How did the first luminous structures form, and how did they evolve and influence the gas around them? Exploring the reionization era opens up a new chapter of our Universe's story - a chapter that promises to connect the dots between our past and present.

1.1.1 Cosmic History

As the Universe expanded and cooled after the Big Bang, electrons and protons eventually combined to form neutral hydrogen atoms. At the young age of $\sim 380,000$ years, the Universe's ordinary baryonic content was almost entirely neutral hydrogen, while most of its total matter was dark matter ([Loeb & Furlanetto 2013](#)). Then, for the next several hundred million years, the *Dark Ages* proceeded, with concentrations of dark matter setting the foundations for the formation of the first luminous structures. More specifically, the tiny, primordial density fluctuations that were established at the release of the CMB grew with inflation and the expansion of the Universe. The densest regions then collapsed to form dark matter halos, inside of which hydrogen gas could cool, condense, and fragment into stars ([Dodelson 2003](#)).

The first luminous structures are thought to have formed at an age of ~ 200 million

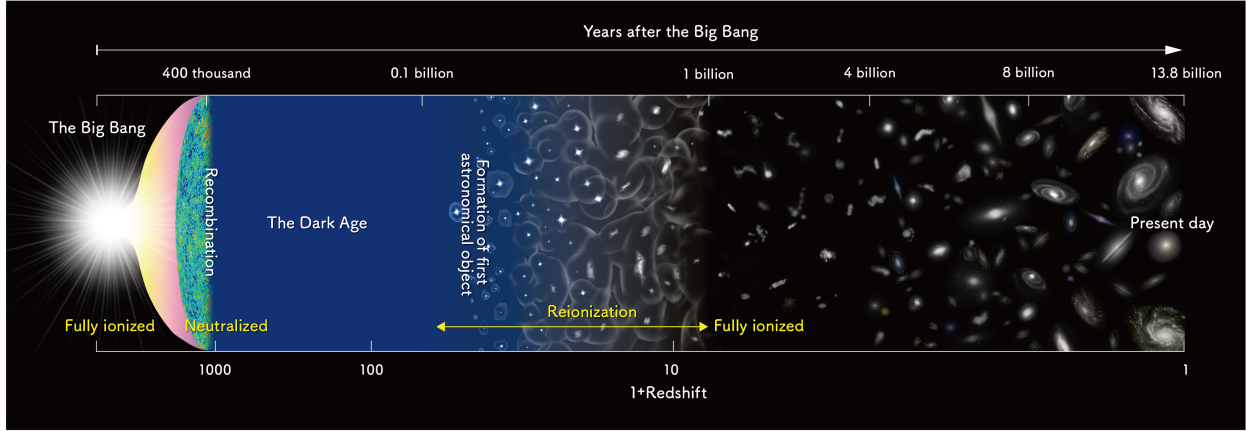


Figure 1.1: Timeline of the history of the Universe. The Epoch of Reionization marks the era when the first stars and galaxies formed and ionized the neutral hydrogen in the Universe. Image credit: NAOJ.

years ($z \sim 20$) and are predicted to have been massive stars with high luminosities and large ionizing powers (Loeb & Furlanetto 2013). The ionizing photons from the first stars carved out pockets of ionized hydrogen gas around the densest, most massive dark matter halos, and as the number of sources grew, an increased number of ionized bubbles emerged and overlapped. Eventually, the first generations of stars and galaxies succeeded in ionizing most all of the neutral hydrogen in the Universe, with reionization complete by about one billion years after the Big Bang ($z \sim 6$) (Furlanetto et al. 2006).

The exact timescale and details of the reionization process, which are shown within the context of the history of the Universe in Figure 1.1, are current research questions in the field of cosmology. The physics of reionization depends on several factors, including the nature of the first stars (masses, luminosities, ionizing photons) and the surrounding gas (efficiency of the ionizing photons, feedback effects). Turning the argument around, deep investigations of the reionization era would lead to new understandings about the properties of the first stars and the intergalactic medium (IGM). There are several ways to approach the study of this epoch, with CMB measurements working to constrain the duration of reionization, galaxy measurements unveiling the end of reionization, and direct hydrogen measurements attempting to map out the changing nature of the gas over time. All of these probes serve to illuminate this watershed era between a Universe dominated by darkness and a Universe defined by light.

1.1.2 CMB and Galaxy Measurements

There are several observational probes of the reionization epoch, and we highlight two broad categories in this section. The first is the study of CMB anisotropies, which carry with them an imprint of the early Universe from the time of its release. But that's not the only

imprint it has - CMB photons can scatter off of free electrons after reionization, and these scatterings leave behind polarization and temperature imprints (Haiman & Knox 1999). For example, the amplitude of the CMB is sensitive to scatterings, as an increased number of scatterings is akin to mixing different parts of the CMB together as photons are scattered in all directions. In other words, this scattering washes out anisotropies in the CMB and lowers its overall amplitude.

A useful parameter to quantify the amount of electron scattering that occurs is the optical depth, τ_{es} , defined as:

$$\tau_{es} = \int n_e \sigma_T dl, \quad (1.1)$$

where n_e is the number density of free electrons, σ_T is the Thompson cross-section, and the integral is taken over a proper length dl . Once reionization begins, the number of free electrons increases, contributing to increasingly higher values of τ_{es} . Hence, an earlier start for reionization would yield higher optical depths than a late reionization scenario.

Observations of the CMB by WMAP and Planck have placed constraints on the optical depth parameter (Hinshaw et al. 2013; Planck Collaboration et al. 2016), with the more recent Planck result suggesting a value of $\tau_{es} \sim 0.07$. This value suggests that reionization ends at a redshift of $z \sim 6$, with instantaneous reionization (“mean” reionization) at $z \sim 8.8$ (Planck Collaboration et al. 2016).

Currently, the results from CMB measurements are in agreement with a second powerful probe of EoR — broadly speaking, that of galaxy observations. This probe comes in many flavors. For example, the spectra of distant quasars at high redshifts can illuminate the end of reionization. Quasars, being extraordinarily bright and energetic objects, are detectable at very far distances and their spectra reveal the amount of absorption their light has undergone due to neutral hydrogen. While nearby quasar spectra exhibit sharp absorption lines, distant ones show the Gunn-Peterson trough, implying that the quasar light was entirely suppressed by hydrogen absorption (i.e., neutral hydrogen existed). Studying the absorption features of quasars at different redshifts implies that reionization has indeed ended by $z \sim 6$ (Becker et al. 2001).

In addition to quasar observations, high-redshift galaxy observations can also reveal important characteristics about the state of the IGM. Namely, distant star-forming galaxies can be detected using a variety of techniques, such as narrow-band imaging to find Lyman- α emitters (radiation that is produced by recombination near young stars) or broad-band observations to find Lyman-break galaxies (spectral breaks associated with absorption by neutral hydrogen). High-redshift galaxy observations can then be used to construct luminosity functions (number of stars per luminosity interval) and star formation histories, which in turn impact the evolution of the IGM.

More specifically, if star-forming galaxies dominated the reionization process, then the ionization rate can be related to the following star-formation parameters:

$$\dot{n}_{\text{ion}} = f_{\text{esc}} \xi_{\text{ion}} \rho_{\text{SFR}}, \quad (1.2)$$

where \dot{n}_{ion} is the cosmic ionization rate, f_{esc} is the escape fraction of photons into the IGM, ξ_{ion} is the rate of production of ionizing photons for a stellar population, and ρ_{SFR} is the star formation rate density. All three parameters influence the rate at which the IGM is ionized, and the star formation rate density is able to be constructed from galaxy luminosity functions. For example, [Robertson et al. \(2015\)](#) used data from the Hubble Space Telescope to construct a star formation rate history out to high redshifts, backing out an optical depth parameter that is consistent with that of Planck.

While galaxy measurements can be used to constrain the EoR, they are ultimately doing so by unveiling the properties of old, distant stars and galaxies. A similar, new technique that also aims to reconstruct the histories of the first luminous structures is observing nearby, metal-poor Local Group galaxies. Called “galactic archaeology,” observations of nearby star-forming ancestors can be used to constrain the faint-end slope of the luminosity function. Determining the shape of this function has important implications on the number of galaxies needed to drive reionization and the types of sources dominating this epoch ([Weisz & Boylan-Kolchin 2017](#)). Additionally, studies of nearby metal-poor stars and galaxies can provide insight into the contents of the first generation of stars and the dynamics of high-redshift star formation, as observations of ultrafaint dwarf galaxies around the Milky Way suggest they are relatively clean tracers of the first generations of stars ([Loeb & Furlanetto 2013](#)).

Galaxy observations for reionization studies have been primarily driven by observations taken by the Hubble Space Telescope. In the coming years, the James Webb Space Telescope (JWST), a 6.5 m infrared space telescope, will be optimally primed for the detection of faint galaxies, including galaxies whose roots extend as far back as the cosmic dawn and who may exhibit signatures of first generation Population III stars. In addition to JWST, several large infrared ground telescopes are also underway, including the European Extremely Large Telescope (EELT), the Giant Magellan Telescope (GMT), and the Thirty Meter Telescope (TMT).

Although both CMB measurements and galaxy observations have much to look forward to, they currently each have their limitations. For example, CMB measurements can only reveal the integrated quantity of τ_{es} , therefore unable to provide insight into the evolution of reionization as it progresses over time. Similarly, galaxy observations are currently limited by sensitivity, able to hover only around the tail end of the reionization era. A different, but complimentary, probe is needed to unlock the entire window into the EoR.

1.1.3 Measurements of HI

A direct measurement of neutral hydrogen gas over time would provide a fundamental way to track the IGM over the reionization process. Such a probe, which is made possible by the spin-flip transition of hydrogen, is a powerful technique that allows the tracing of gas over time, and it is this technique that serves as the basis for the remainder of this thesis ([Furlanetto et al. 2006; Barkana & Loeb 2008; Morales & Wyithe 2010; Pritchard & Loeb 2010; Pritchard & Loeb 2012](#)).

The spin-flip transition of neutral hydrogen occurs when a hydrogen atom changes energy

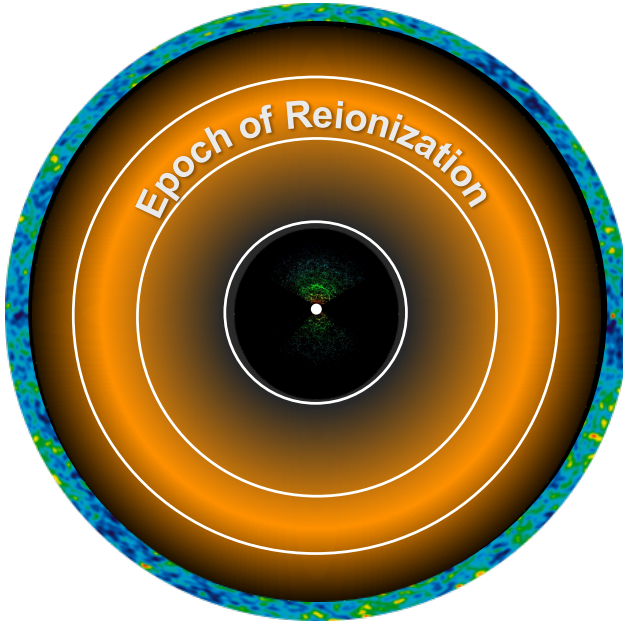


Figure 1.2: A cartoon diagram of the observable Universe, centered on us. Close-by, galaxy observations have mapped out cosmic web structure in our nearby Universe (image credit: SDSS). Far-away, the cosmic microwave background is observed at a redshift of $z \sim 1100$ (image credit: WMAP). The Epoch of Reionization represents a largely unexplored era between the two, and can be probed by measuring red-shifted 21 cm radiation from neutral hydrogen.

state between two hyperfine levels. Namely, if a hydrogen atom moves from an aligned energy state (the proton and electron have parallel spins) to an anti-aligned state (the proton and electron have antiparallel spins), the energy difference is released in the form of a photon with a wavelength of 21 cm.

Because this transition has a well-defined wavelength, the signal can be directly mapped to a distance, or redshift, by measuring its wavelength upon detection. For example, a 21 cm photon that was initially emitted at a redshift of $z = 6$ would have expanded by a factor of $(1 + z)$ due to the expansion of the Universe and be 1.5 m long when it arrives at our telescopes. Hence, observing longer wavelengths of the hydrogen signal means that it has traveled for a greater distance (and has stretched out more) and thus comes from farther away at a higher redshift. This means that the 21 cm signal is a powerful tracer of neutral hydrogen at any distance (i.e., as a function of time), as long as it exists. This technique is especially compelling because it allows the direct exploration of the EoR as reionization occurs, whereas CMB measurements and galaxy measurements surround this era from the beginning and end only, respectively (Figure 1.2).

In practice, the 21 cm signal is encapsulated by the quantity T_{spin} (spin temperature), which measures the relative number of hydrogen atoms in the excited (aligned) versus ground (anti-aligned) spin-flip state. A high spin temperature means that the hydrogen gas is more

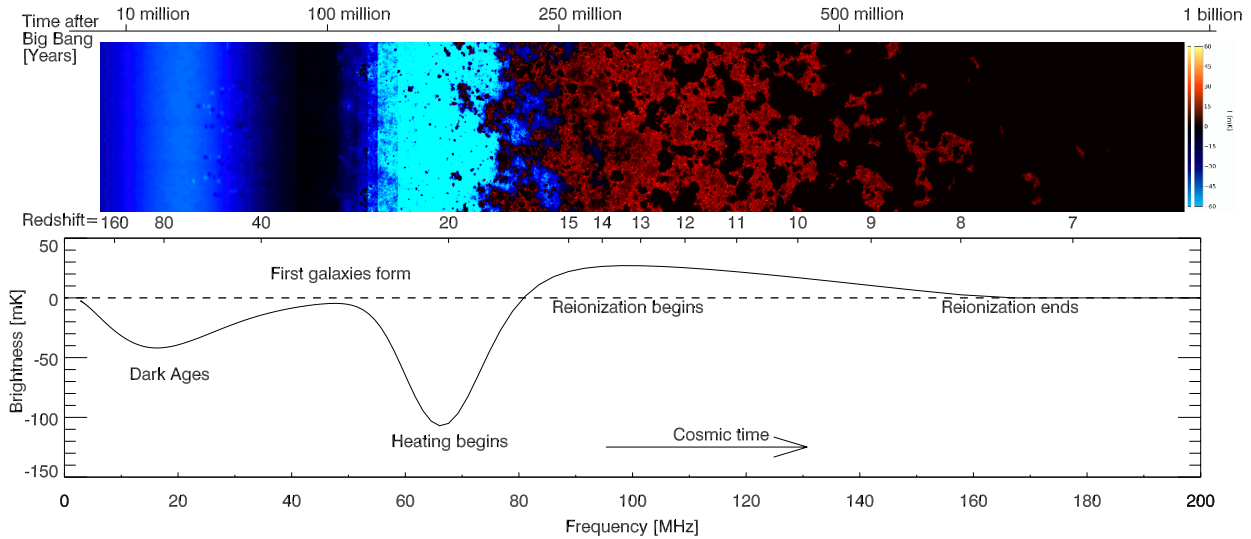


Figure 1.3: The evolution of the global 21 cm signal, starting with the Dark Ages, through galaxy formation and reionization (image credit: [Pritchard & Loeb \(2012\)](#)). The work in this thesis mainly focuses on a redshift range of $6 < z < 12$ when reionization is expected to progress and complete.

likely to emit 21 cm photons, whereas a low T_{spin} implies that the gas is more likely to absorb 21 cm photons.

The spin temperature is always measured with respect to the temperature of the CMB (T_{CMB}), which serves as a backlight for our measurement. During different stages of our cosmic history, T_{CMB} and T_{spin} take turns in the spotlight, with the *differential brightness temperature* δT_b describing their evolution:

$$\delta T_b \propto (1 + \delta_b)x_{HI} \left(1 - \frac{T_{\text{CMB}}}{T_{\text{spin}}}\right). \quad (1.3)$$

Equation (1.3) captures the EoR signal that 21 cm experiments seek to measure, where δ_b is the fractional over-density of matter and x_{HI} is the fraction of neutral hydrogen (1 if all neutral, 0 if all ionized). The differential brightness temperature can be measured in multiple ways — in Chapter 1.2 we explain how interferometry (multiple telescopes) can be used to measure the correlations of δT_b on various spatial scales on the sky. Here we describe the evolution of the sky-averaged δT_b , called the *global signal*, in order to summarize how it is expected to behave during our cosmic dawn and through reionization.

A theoretical prediction for the evolution of δT_b is shown in Figure 1.3. At the very far left, a cool, neutral IGM remains after recombination and the release of the CMB. Residual electrons collide off of both CMB photons and the hydrogen gas, driving couplings between T_{gas} and T_{CMB} , and T_{gas} and T_{spin} , respectively. Hence, we expect to see no signal ($\delta T_b = 0$) at this time.

During the Dark Ages, collisions still couple T_{gas} and T_{spin} , but Compton scattering

becomes rarer as the CMB dilutes with the expansion of the Universe. While the CMB dilutes as $T_{\text{CMB}} \propto 1/a$, where a is the scale factor, the gas now follows an adiabatic expansion ($T_{\text{gas}} \propto 1/a^2$). Thus, the gas cools quicker than the CMB, and since it is still coupled to the spin temperature, $T_{\text{spin}} < T_{\text{CMB}}$ and the signal is expected to be seen in absorption. By the time the first galaxies begin forming, however, the gas is expected to be so dilute that it is no longer coupled to the spin temperature. The spin temperature therefore couples once again to the CMB, and no signal is produced.

As the first stars in the first galaxies begin emitting Lyman- α photons, they are resonantly scattered off of hydrogen via the Wouthuysen-Field effect (the absorption and emission of Lyman- α photons redistributes the spin-flip states), coupling T_{spin} and T_{gas} (Pritchard & Loeb 2010). The gas, still cool from adiabatic expansion, implies that $T_{\text{spin}} < T_{\text{CMB}}$ and the signal is seen in absorption. Eventually, due to their long mean free paths, x-rays from the first sources are thought to be the primary drivers behind heating of the cooled, low-density gas (Furlanetto et al. 2006). This drives both the gas and spin temperatures above that of the CMB, where the signal is expected to be seen in emission for the first time.

Finally, even though the timing and details of reionization are unknown, UV photons from the first luminous structures are believed to eventually ionize all the neutral hydrogen, leaving no signal to be detected by a redshift of $z \sim 6$.

The shape of the global signal holds important science implications about our early Universe. For example, the timing of the heating trough reveals the types of sources responsible for heating (i.e., late heating implies harder x-ray spectra for x-ray binaries, as shown in Fialkov et al. (2014)). It also contains information regarding the sizes of the dark matter halos hosting those first sources and the cooling mechanisms responsible for star formation (Fialkov et al. 2014). The shape of the absorption feature is also dependent on a number of factors, such as x-ray and Lyman- α emissivities, which in turn are dependent on the nature of the first sources and properties of star formation. For high Lyman- α production rates, a deep trough would be present due to strong couplings between T_{spin} and T_{gas} as the gas cools. An even more pronounced absorption signature, such as the first tentative detection from the Experiment to Detect the Global Epoch of Reionization Signature (EDGES), requires additional physical explanations beyond known physics and commonly accepted scenarios (Bowman et al. 2018).

If the global signal’s primary absorption feature unlocks clues about the first sources, the reionization peak and its subsequent decay hold the key for understanding the evolution of the neutral fraction x_{HI} . Namely, a direct measurement of δT_b during this time would shed light about the duration and rate of the reionization process, which in turn can be translated into an evolution for x_{HI} . A long reionization duration, for example, would yield a slowly varying neutral fraction evolution, while a more instantaneous reionization would produce a sharp drop-off feature (Pritchard & Loeb 2010). One thing is for certain though — as the field continues to investigate our cosmic dawn and the EoR through HI measurements (both the global signal and statistical fluctuations), we can expect to learn much about the constituents that make up the Universe and their complex interactions during this era.

1.1.4 This Thesis

Although 21 cm observations promises an uninterrupted window into the EoR, from which we can learn much about galaxy formation and the properties of the IGM, there are many challenges facing this field of cosmology. In general, the 21 cm signal is extremely faint, with bright foregrounds (mostly synchrotron radiation from our own Galaxy) and radio interference easily overshadowing the target signal. As a consequence, instruments need to be extremely well-understood, precisely calibrated, and sensitive enough for a successful detection. In addition, analysis techniques must be innovative and rigorously construed so as to be able to extract clean and accurate measurements.

In this thesis, I present work associated with data from radio interferometers seeking to measure 21 cm fluctuations during the EoR. While a confirmed detection by an interferometer remains elusive at this time, this work serves as a huge leap forward in working with large datasets and extracting measurements of the cosmological signal with confidence. The rest of this thesis thus focuses on the characterization of data from large telescope arrays in order to place accurate, stringent limits on the EoR signal. This field is still young, and the work in this thesis serves as a foundation of what promises to be an eye-opening adventure to-come.

1.2 Interferometry

Multiple radio telescopes (i.e., an interferometer) can be used in combination to probe 21 cm fluctuations. Rather than a single element, or aperture, many antennas can be used to increase the effective aperture size of the telescope.

As a simplistic example, two antennas may observe the same sky but each receives the sky signal at slightly different times, with a time delay determined by the antenna spacing, or baseline orientation and length, with respect to the sky. The two voltage streams from the antennas can then be correlated to form an output response with an amplitude dependent on the sky's intensity and a phase dependent on the time delay between the two elements and the frequency of the light. The power received by this baseline, as we will see, represents one sample in the large "synthesized" aperture of the interferometer. Knowledge of the entire sky can be built up by having a large number of antennas and many different types, and copies, of baselines.

1.2.1 The Visibility Equation

The output measurement from correlating signals between two antennas is called a *visibility*. The visibility can be written as:

$$V_{ij}(\nu) = S(\nu) e^{-2\pi i \frac{\vec{b}_{ij} \cdot \hat{s}}{\lambda}}, \quad (1.4)$$

where i and j represent a pair of antennas, $S(\nu)$ is the sky flux density, \vec{b}_{ij} is the baseline vector, \hat{s} is a unit-vector in the direction of a source in the sky, and λ is the wavelength of the

signal. The fractional term in the exponential reflects the changing number of wavelengths between the two antennas as a signal goes in and out of phase as the source passes overhead. The entire exponential term represents the phase of the visibility, which can also be described as the fringe pattern, or diffraction, or interference pattern, between two antenna elements.

Equation (1.4) represents a visibility measurement for one direction on the sky. In practice, we compute the integrated visibility over the entire angular sky $d\Omega$:

$$V_{ij}(\nu, \Omega) = \int A(\nu, \Omega) I(\nu, \Omega) e^{-2\pi i \frac{\vec{b}_{ij} \cdot \hat{s}(\Omega)}{\lambda}} d\Omega, \quad (1.5)$$

where the amplitude component has been broken up into a primary beam component $A(\nu, \Omega)$ and sky intensity component $I(\nu, \Omega)$. The primary beam describes the power pattern of an antenna element and determines its field of view. The total power received by an antenna can therefore be thought of as a combination of the intensity distribution on the sky and how receptive the antenna is, or more specifically, the convolution between the two terms (Thompson et al. 2001).

The visibility equation can be re-interpreted as the 2-dimensional Fourier-transform of the sky, or a sample of the uv -plane, where u and v are sine-waves in a 2D image. In other words, every baseline measures a different Fourier-mode of the sky. To form an image, the Fourier-transform of a visibility would produce a *dirty image* of the sky, from which the true sky can be reconstructed by de-convolving out information from the antenna beam. In this thesis, however, we focus on the 3D Fourier-transform of the sky, or the power spectrum (Chapter 1.2.2), instead of making images. Hence, we work directly with visibilities as a starting point, which has already taken two Fourier-transforms for us.

1.2.2 The 21 cm Power Spectrum

In this thesis, we focus on cross-correlations, or power spectral measurements, of visibilities. Recalling that we seek to measure the differential brightness temperature on various spatial scales of the sky, we can form the quantity:

$$\langle \delta \tilde{T}_b(\vec{k})^* \delta \tilde{T}_b(\vec{k}) \rangle = (2\pi)^3 \delta^D(\vec{k} - \vec{k}') P_{21}(\vec{k}), \quad (1.6)$$

where $\delta \tilde{T}_b(\vec{k})$ is the Fourier-transform of the differential sky brightness as a function of cosmological wavenumber \vec{k} (i.e., our visibility measurement, up to scaling factors), δ^D is the Dirac-delta function, and P_{21} is the 21 cm power spectrum quantity we are interested in eventually forming.

Simply speaking, because our visibility measurements have already taken two spatial Fourier-transforms out of the three needed for a 3D power spectrum, we need only to take one last Fourier-transform (along frequency), and then multiply and average the visibilities together for a given baseline in order to compute a power spectral measurement. Having repeated baseline copies then increases the sensitivity to a given Fourier-mode on the sky, while having different types of baselines makes it possible to measure multiple Fourier-modes

and build up an image of the sky. Since the EoR signal is expected to be present everywhere on the sky, in this work we focus on the former technique in order to maximize our sensitivity to the cosmological signal.

We note that the wavenumber \vec{k} can be broken up into a perpendicular component \vec{k}_\perp and a parallel component k_\parallel , where \vec{k}_\perp is proportional to the (x,y) spatial coordinates on the sky and k_\parallel is proportional to the line-of-sight direction on the sky (i.e., frequency). Every unique baseline probes a single \vec{k}_\perp , and it's worth noting that, because we focus on redundant baselines in the analysis to follow, most of our power spectrum sensitivity comes from the frequency-direction. Accounting for cosmological distance, a 1D wavenumber has units of Mpc^{-1} , so that the 3D power spectrum has units of $\text{mK}^2 \cdot \text{Mpc}^3$. Visibility measurements typically have units of Janskys.

Just as the shape of the global signal provides insight about the early Universe, the shape of the cross-power spectrum, as defined by Equation (1.6), also delivers a wealth of information. Figure 1.4 shows the 21 cm “dimensionless” power spectrum $\Delta^2(k)$ (units of mK), defined as:

$$\Delta^2(k) = \frac{k^3}{2\pi^2} P_{21}(k), \quad (1.7)$$

as a function of the magnitude of k . This figure shows the expected evolution of the power spectrum, where the overall signal moves to small scales (large k) as more hydrogen becomes ionized (the large regions of neutral hydrogen turn into smaller and smaller pockets). This effect can be seen by both the steepening of the spectrum as the neutral fraction decreases, and the time-evolution of the spectrum at a specific (large) k .

The 21 cm power spectrum therefore encodes important information about the spatial and temporal evolution of reionization, and the shape of the spectrum can be directly mapped to sizes of the ionized bubbles as they grow. Additionally, the power spectrum, which is a function of the differential brightness temperature, can be used to constrain both T_{spin} (and T_{gas} , since they're coupled during this era) and x_{HI} via Equation (1.3). It is thus a powerful tool for unlocking the properties of the IGM.

1.2.3 Calibration

We now transition to a brief overview of key data processing steps that are often standard routines when going from visibilities to power spectra. We speak broadly about these steps in this chapter, and go into detail about them for specific experiments in later chapters.

As discussed previously, an interferometer measures a visibility for every baseline pair and every time integration. Repeated baseline types and multi-day observations can be stacked to gain sensitivity to Fourier-modes on the sky. However, ensuring clean measurements at EoR sensitivities requires many other crucial processing steps, including calibration, which we give an overview of in this section.

We've seen that the visibility measurement is dependent on the sky, baseline, and antenna beam, but it is also affected by instrumental systematics. For example, certain components

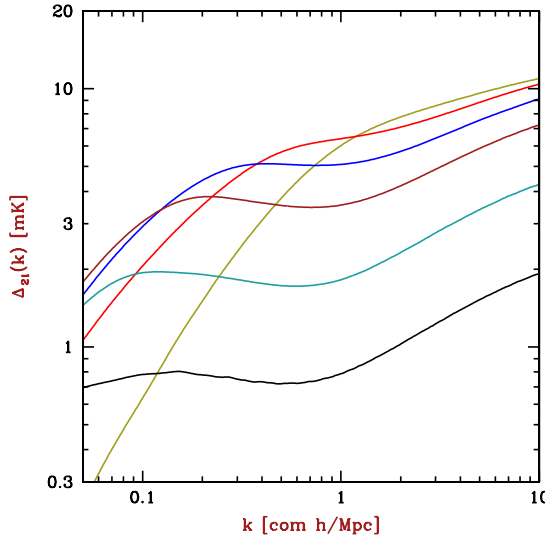


Figure 1.4: The theoretical evolution of the cross-21 cm power spectrum for a specific model (image credit: [Barkana \(2009\)](#)), where the neutral fraction $x_{HI} = 10\%, 30\%, 50\%, 70\%, 90\%$, and 98% from top to bottom at large k . This figure shows the expected evolution of the power spectrum which interferometers seek to measure.

in the signal chain of an instrument can contribute variable noise, losses can arise from reflections, and blockage and scattering may occur. These are all effects that must be considered in order to accurately extract the EoR signal.

Many of these effects can be mitigated through precise calibration. There are two main types of calibration used by 21 cm interferometers: *redundant* calibration and *absolute* calibration. We will briefly describe each here.

Redundant calibration is a type of calibration based on the redundant nature of baselines. For experiments like PAPER and HERA, which have many repeated copies of baselines, redundant calibration can be used to bring all identical baselines into agreement (i.e., it calibrates out deviations between baselines of the same type). This calibration is a powerful technique because it does not use any knowledge of the sky, yet can correct for instrumental-induced gain and phase effects brought on by differences in the signal chain attributable to antennas, cables, and receivers ([Liu et al. 2010](#)).

Mathematically, the visibility v_{ij} of every baseline can be written as:

$$v_{ij} = g_i^* g_j y_{ij} + n_{ij}, \quad (1.8)$$

where g_i and g_j are the complex gains of each antenna, y_{ij} is the “true” model visibility for that particular baseline type, and n_{ij} is noise. The goal of redundant calibration is to solve for the gain of each antenna and the “true” visibility of each baseline type. This can be accomplished by setting up a system of linear equations containing every visibility measurement (the method used by PAPER and HERA is detailed in Chapter [3.1](#)). If there

are more measurements than the sum of the number of unique baselines and antennae, then it is a solvable system.

The complex gains can be further broken down to be written as $g_i = e^{\eta_i + i\phi_i}$ (Liu et al. 2010). In other words, by solving for the gains, we are solving for both an amplitude component and a phase offset for each antenna. The gains can then be divided out of every visibility measurement, producing redundantly-calibrated measurements across the whole array.

While redundant calibration is a clever technique for the internal calibration of an interferometer, the calibrated visibility measurements are still on an arbitrary gain scale that has not been matched up to the sky. Hence, absolute calibration refers to using sources in the sky of known brightness (or sky models) in order to solve for the two remaining internal degrees of freedom: an overall gain and an overall phase. Interferometers typically use a standard self-calibration routine to accomplish this, where y_{ij} is known for specific sky sources.

Ultimately, calibration is a crucial step in preparing interferometric data for a power spectrum analysis. A precisely-calibrated instrument will result in cleaner data from which the EoR signal can be accessed.

1.2.4 Foreground Filtering

Arguably the largest challenge of processing 21 cm data is in removing bright foregrounds. There are several techniques to do this, which fall into two main categories: foreground subtraction and foreground avoidance. The former consists of modeling and subtracting out foreground sources, while the latter involves making EoR measurements in a domain where foregrounds are minimal.

For interferometers with imaging capabilities, foreground removal techniques include modeling approaches to spatially localize and remove contaminants (e.g., Santos et al. 2005; Wang et al. 2006; Jelić et al. 2008; Liu et al. 2009; Bowman et al. 2009; Harker et al. 2009; Chapman et al. 2016). This can be done by fitting polynomials to data or by using non-parametric methods, which make fewer assumptions about the form of the foregrounds. While foreground subtraction would be ideal if done accurately, modeling is difficult and subtraction poses the risk of cosmological signal loss.

The other method commonly used, foreground avoidance, is a strategy employed by both PAPER and HERA. Foreground avoidance was originally suggested as an alternate method to the subtraction method, which has stringent requirements in order to yield uncontaminated results. In order to understand foreground avoidance, we must first define the “EoR Window”.

A 3D power spectrum can be split into two directions along k_{\perp} and k_{\parallel} , which correspond to modes perpendicular to the line-of-sight and along the line-of-sight, respectively. In this two-dimensional space, there are two main regions — one relatively free of foregrounds (the “EoR Window”) and one contaminated by foregrounds (the “wedge”), as shown in Figure 1.5 (e.g., Datta et al. 2010; Vedantham et al. 2012). We can see this by thinking of the k_{\parallel} direction to be akin to the physical time delay associated with light hitting two antennas (a

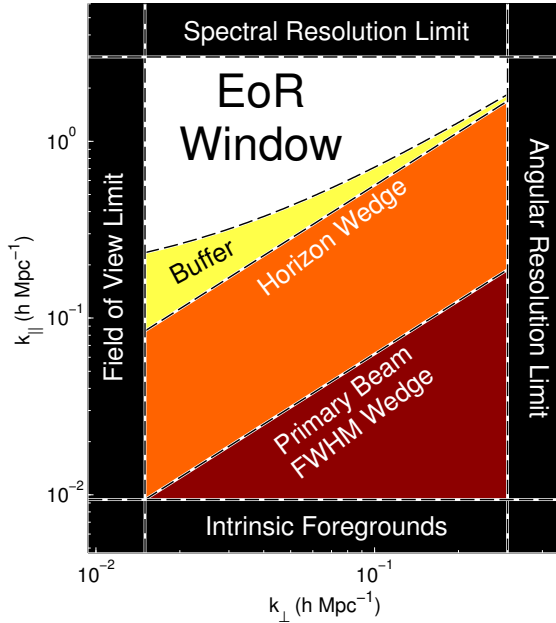


Figure 1.5: A cartoon diagram of the “EoR Window” and “wedge” of foreground contamination in Fourier space (image credit: [Dillon et al. \(2015b\)](#)). A foreground avoidance approach makes power spectrum measurements in the window, while a foreground subtraction approach subtracts out foregrounds so that measurements can be made in the wedge. The overall power spectrum measurement space is limited by an interferometer’s field of view and angular resolution along the horizontal axis, and spectral resolution and intrinsic foregrounds along the vertical axis.

good approximation, especially for short baselines). As k_{\perp} , which is proportional to baseline length, increases, the maximum time delay also increases because it is set by the length of the baseline (i.e., a maximum delay occurs when a source is at the horizon; therefore, the time delay is simply the time it takes for the light to travel the distance of the baseline). Hence, the “wedge” is formed, representing a region where smooth-spectrum foregrounds are expected to be contained. Said differently, foregrounds are expected to be bound by the light-crossing time between two antennas, and therefore there is a maximum limit for k_{\parallel} (time delay) given a k_{\perp} (baseline).

Delay-filtering is the process by which foregrounds within the wedge are filtered out, leaving a relatively clean window behind from which the cosmological signal can be extracted ([Parsons et al. 2012](#)). This approach limits the number of modes for which the measurement can be made and can suffer from some foreground leakage as explained in Chapter 2.5, but its advantages include its simplicity and conservativeness (i.e., it leaves all the cosmological signal within the window in tact).

Whether it’s avoidance or removal, there have been many approaches at tackling the challenge of foregrounds (summarized in [Chapman et al. \(2016\)](#)). But, regardless of the

method used, removing Galactic and extragalactic foregrounds from 21 cm data is absolutely a critical step for analyses seeking the EoR signal.

1.2.5 Fringe-rate Filtering

The final analysis technique to introduce in this section is fringe-rate filtering, a filtering scheme carried out in a domain which is the Fourier-dual to time. This type of filtering aims to optimize the process of combining time-ordered data and has been investigated in [Roshi & Perley \(2003\)](#), [Parsons & Backer \(2009\)](#), [Offringa et al. \(2012\)](#), and [Parsons et al. \(2016\)](#).

A “fringe-rate” is the rate at which the sky moves relative to the fringe pattern of an interferometer. As sources pass overhead, they walk in and out of the interference pattern of two antennas, and the rate at which this movement happens is dependent on the source’s declination and hour angle. For example, a source located near a celestial pole has a zero fringe-rate, as it does not appear to move in the sky as the Earth rotates. However, a source located on the celestial equator will have a maximum fringe-rate set by the rate of Earth’s rotation. The sky can therefore be decomposed into fringe-rate bins, each of which forms a concentric circle of constant fringe-rate around the celestial sphere.

One initial advantage of filtering in fringe-rate space is that it allows the filtering of noise that is not associated with movement locked on the sky (i.e., filtering out fringe-rates greater than the maximum allowed by the Earth’s rotation). This excess noise can come from the instrument itself or from signals with an origin not on the sky. Additionally, one can up-weight and down-weight certain portions of the sky by choosing different linear combinations of fringe-rates ([Parsons et al. 2016](#)). This allows what is effectively a beam-sculpting operation, where the most sensitive parts of one’s beam can be up-weighted compared to others.

A third advantage of this type of filtering is that it can also be used to integrate visibilities in time. Depending on the shape of the filter in the fringe-rate domain, the effect in the time domain can be an averaging operation along time. This is advantageous because it allows an optimal way of combining measurements (by weighting fringe-rates differently based on signal-to-noise ratios in each fringe-rate bin, for example) compared to a more traditional boxcar average, which does not use information from individual fringe-rate bins.

Broadly, fringe-rate filtering can be thought of as a tailored filtering step that can increase the sensitivity of a measurement by differentiating between noise- and signal-like modes in data. When carefully chosen, a fringe-rate filter can enhance modes containing emission from the celestial sphere, where the 21 cm signal lies.

1.3 Instruments

The recent exploration of our cosmic dawn has led to the development of multiple experiments that are aiming to detect the 21 cm signal from neutral hydrogen during reionization. In this section we will first highlight the two main radio interferometers whose data is used

in this thesis, and then discuss other similar experiments along with the current status of the field.

1.3.1 The Precision Array for Probing the Epoch of Reionization

The Precision Array for Probing the Epoch of Reionization (PAPER) is a first generation EoR experiment. Its history dates back to 2007, when an initial four dipole antennas observed the sky from Western Australia. A year later, the array increased to eight stations and moved to Green Bank, West Virginia. These first two deployments are summarized in [Parsons et al. \(2010\)](#) and were used to characterize important aspects of the instrument, including system performance, beam models, instrumental temperatures, and sensitivity to radio frequency interference (RFI).

PAPER then moved to the Karoo Desert in South Africa, near the Square Kilometre Array South Africa (SKA-SA). The PAPER array doubled in size each year, starting with 32 antennas in 2011 and ending with 128 a few years later. PAPER’s observing seasons using these three arrays (PAPER-32, PAPER-64, and PAPER-128) have primarily been used to develop analysis techniques, understand instrumental design, and begin to place limits on the EoR and connect them to science implications.

A brief overview of the PAPER instrument and digital backend follows. The PAPER dipole itself (Figure 1.6) is made from two rods of copper sandwiched between two aluminum disks. The sizes of each are fine-tuned to produce an antenna frequency response between 100-200 MHz. Each PAPER antenna is sensitive to two orthogonal polarizations, those being the East/West and North/South directions (XX and YY linear polarizations) given the antenna’s orientation on the ground. A grounding structure, made of wire-mesh and held in place by PVC pipes, is both underneath the dipole and surrounds it as four angled panels. The design of the antenna’s framework was driven by the desire to produce spectrally and spatially smooth beam responses as discussed in [Parsons et al. \(2010\)](#) and [Pober et al. \(2012\)](#). Altogether, an entire PAPER dipole measures about 2 m on each side and sits still while the Earth’s rotation moves the sky above (“drift-scan” mode). When photons hit the dipoles’ copper rods, electrons are excited and their movement turns the electric field into a voltage that can be measured.

In short, PAPER’s analog system consists of a balun attached to each dipole element (which measures the voltage and amplifies the signal) and coaxial cables which transport the antenna signals. The signals then travel to dual-channel receiver boards which are cooled inside thermal enclosures in order to prevent the introduction of high gains from temperature fluctuations. The receivers both amplify and filter (in frequency) the signals before sending them to the digital system.

PAPER’s digital system is housed inside a refrigerated container on the observing site. The bulk of the processing is carried out by a series of real-time digital FX correlators which cross-correlate pairs of antenna signals to form visibility measurements. More specifically, the FX correlators comprise of “F-engines” which digitize, down-convert, and channelize antenna inputs, a switch that divides the data into frequency subsets and routes the packets, GPUs

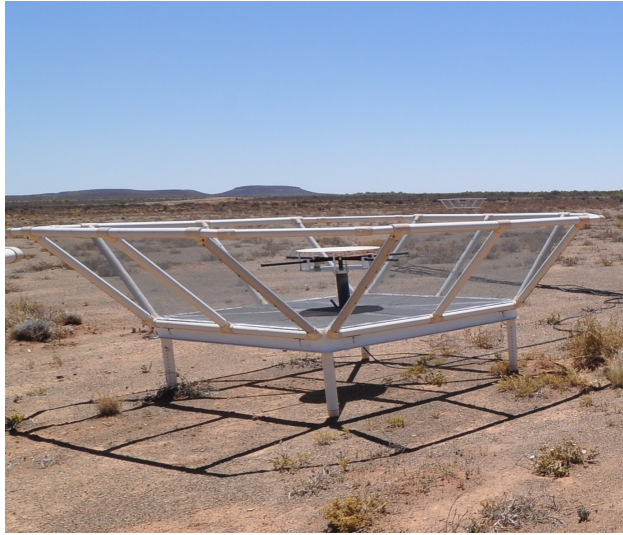


Figure 1.6: A PAPER antenna in the Karoo Desert in South Africa. A dual-polarization dipole sits at the center, surrounded by wire mesh panels that measure 2 m on each side.

which cross-multiply signals from all antenna pairs and integrate in time (“X-engines”), and finally another switch and computer which collect the data, writes it to disk, and sends the final products over an ethernet connection as “raw” visibility data products that are ready to be analyzed.

Much of PAPER’s digital signal processing (DSP) system has been made possible due to the development of hardware by the Center for Astronomy Signal Processing and Electronics Research (CAPSER). We rely on their Field-programmable Gate Array (FPGA) processors which can quickly perform the fast Fourier-transforms required to produce visibilities. The development of FPGA’s into PAPER’s DSP system has been critical in allowing for the scalable expansion of the array.

PAPER’s first power spectrum limits on the EoR came from its 32-element array ([Parsons et al. 2014](#)). PAPER-32 observed in a redundantly-configured layout from 2011-2012, producing a published 2σ upper limit on the 21 cm power spectrum of $(41 \text{ mK})^2$ for $k = 0.27 h \text{ Mpc}^{-1}$ at $z = 7.7$ ([Parsons et al. 2014](#)). This result, while orders of magnitude above predicted EoR signals, was used to generate constraints on the brightness temperature of 21 cm emission for various reionization models and rule out cold reionization scenarios (i.e., some heating of the IGM is necessary by $z = 7.7$ to be consistent with PAPER-32’s results).

PAPER expanded to 64 elements in 2012, keeping its redundant layout in order to maximize power spectrum sensitivity. The analysis and initial results for PAPER-64’s observing season is outlined in [Ali et al. 2015](#), where a 2σ upper limit on the EoR is published as $(22 \text{ mK})^2$ for $0.15 < k < 0.5 h \text{ Mpc}^{-1}$ at $z = 8.4$. A result at this sensitivity can begin to place more interesting limits on IGM heating models and on the temperature of the IGM during this time ([Pober et al. 2015](#)).

From 2013-2015, PAPER-128 marked the last era for the PAPER experiment. The data

collected with this array has not been published publicly and work is ongoing to process and analyze this data. While most of this thesis focuses on PAPER-64, specifically on analysis methods developed to revise the initial (incorrect) PAPER-64 results (Chapter 2) and what those new limits should be (Chapter 3), we also present a first-look at PAPER-128 and discuss how PAPER’s final observing season has influenced analysis metrics for next generation experiment HERA (Chapter 4).

The PAPER experiment as a whole has been absolutely fundamental to the growth of the field of 21 cm cosmology. This first generation experiment set a standard for other similar experiments and has provided countless lessons in all aspects of the signal chain. The array may be retired, but its influence will not be forgotten.

1.3.2 The Hydrogen Epoch of Reionization Array

The development of the Hydrogen Epoch of Reionization Array (HERA) was largely driven by the need for increased sensitivity, as even PAPER-128 lacked the collecting area for a significant detection of the EoR. HERA is a second generation EoR experiment currently being built in the Karoo. It features a staged build-out of parabolic dishes with 14 m diameters, with construction beginning in 2015 and an eventual 350 dishes planned to be completed by the end of 2019.

A HERA dish (Figure 1.7) is made up of wire-mesh, PVC pipes, and wooden support structures. The size, shape, and total number of the dishes were chosen in order to optimize sensitivity (i.e., minimize chromatic effects that would leak power into the EoR window), minimize costs, and be easily scalable and robust for a five year lifetime (DeBoer et al. 2017). While work on a new feed design (with a wider bandwidth) is ongoing, the first observations from HERA use recycled PAPER dipoles. Suspended upside-down with a wire pulley-system, the PAPER dipoles are surrounded by a wire-mesh backplane structure that minimizes cross-coupling between antennas while optimizing beam efficiency, frequency response, and polarization match (DeBoer et al. 2017). Similarly, the first stages of the HERA array are using the existing PAPER signal chain and hardware, while work is progressing towards an underground node-based architecture that will house the DSP system and minimize cable reflections by allowing for shorter cable paths.

The configuration of HERA, like PAPER, is highly redundant and optimized for a robust foreground avoidance approach. Because this power spectrum approach requires short baselines (which minimize the wedge), the HERA antennas are densely-packed next to each other into a main core. This core is segmented into three displaced sections, whose sectioning is designed to improve HERA’s imaging ability (Dillon & Parsons 2016). Additionally, there will be 30 outrigger elements joining the full array, allowing for a more complete *uv*-plane coverage and imaging capabilities that can be leveraged for a foreground removal approach. The full HERA array is depicted in Figure 1.8.

The primary science goal of HERA is to make a high-significance detection of the cosmological signal in order to constrain the timing and morphology of reionization. With precision constraints on the EoR, we can begin to understand the role of the first stars and



Figure 1.7: A HERA dish in the Karoo Desert in South Africa. Wire-mesh, PVC pipes, and wooden structures serve as the foundation for the 14 m diameter parabola. A PAPER dipole is suspended upside-down with a wire pulley-system and surrounded by a prototype wire-mesh skirt structure. HERA-350 will use an updated design for its feed; however, HERA’s initial data releases use the old PAPER infrastructure as depicted here.

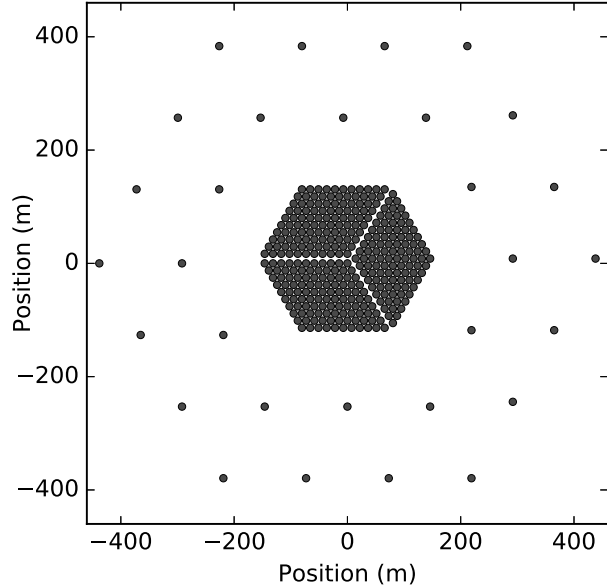


Figure 1.8: The full HERA-350 array (image credit: [DeBoer et al. \(2017\)](#)). The array is comprised of a segmented densely-packed core (to optimize redundancy for a foreground avoidance approach) and surrounding outrigger elements (for imaging capabilities).

galaxies in driving reionization, their complex interactions with their environments, and the evolution of cosmic structure. With the full array and an upgraded feed sensitive from 50–250 MHz, secondary science goals of the instrument include precision cosmology, imaging of the reionization epoch, and an investigation of the pre-reionization heating epoch (DeBoer et al. 2017). HERA, with a collecting area of $\sim 0.1 \text{ km}^2$, is well-poised for these challenges (Pober et al. 2014) and has already undergone numerous tests and simulations to ensure that its design meets specification (Neben et al. 2016; Ewall-Wice et al. 2017; Patra et al. 2018). As the fully realized HERA soon approaches, there is much to look forward to in the coming years from this array.

1.3.3 Other Experiments and Status of Field

Although this thesis focuses mostly on PAPER data and analysis methods that will be used by HERA, these two arrays are not alone in their quest for the EoR. Other radio interferometers which seek to measure statistical power spectra include the Giant Metre-wave Radio Telescope located in India (GMRT; Paciga et al. 2013), the LOw Frequency ARray in Europe (LOFAR; van Haarlem et al. 2013), the Murchison Widefield Array in Australia (MWA; Tingay et al. 2013), the 21 Centimeter Array in China (21CMA; Peterson 2004; Wu 2009), and the Square Kilometre Array in South Africa (SKA; Koopmans et al. 2015).

Several of these experiments have succeeded in placing upper limits on the EoR, including results from the 32-tile MWA (Dillon et al. 2014), 128-tile MWA (Dillon et al. 2015a; Beardsley et al. 2016), GMRT (Paciga et al. 2013), and LOFAR (Patil et al. 2017). PAPER has also previously published results using 32 antennas (Parsons et al. 2014; Jacobs et al. 2015) and 64 antennas (Ali et al. 2015), though we highlight the errors found in PAPER’s analysis pipeline throughout this thesis and thus refer the reader to Chapter 3 for updated results from PAPER.

The work in the 21 cm community that has led to these power spectrum limits (Figure 1.9) has largely revolved around the key challenge of controlling foregrounds and systematics. To accomplish this, significant progress has been made in all aspects of the experimental process, ranging from carefully designed interferometers (Lonsdale et al. 2009; Parsons et al. 2012; Dillon & Parsons 2016), to novel methods for understanding and dealing with foregrounds (e.g., Morales et al. 2006; Datta et al. 2010; Sullivan et al. 2012; Moore et al. 2013; Hazelton et al. 2013; Pober et al. 2013; Liu et al. 2014a; Liu et al. 2014b; Thyagarajan et al. 2015), to statistical analysis techniques for precise calibration and power spectrum estimation (e.g., Liu et al. 2010; Trott et al. 2012; Liu et al. 2014b; Zheng et al. 2014; Dillon et al. 2014; Jacobs et al. 2016). PAPER’s foreground avoidance strategies have, in particular, led to detailed understandings of redundant calibration and the effects of filtering on the EoR window, while MWA’s foreground subtraction techniques have provided complementary improvements in imaging capabilities. While the experiments with published results currently lack the sensitivities needed for an EoR detection, both the delay-filtering and map-making methods, along with hybrid approaches (Trott et al. 2016), have set a strong foundation for controlling foregrounds by future, more sensitive interferometers.

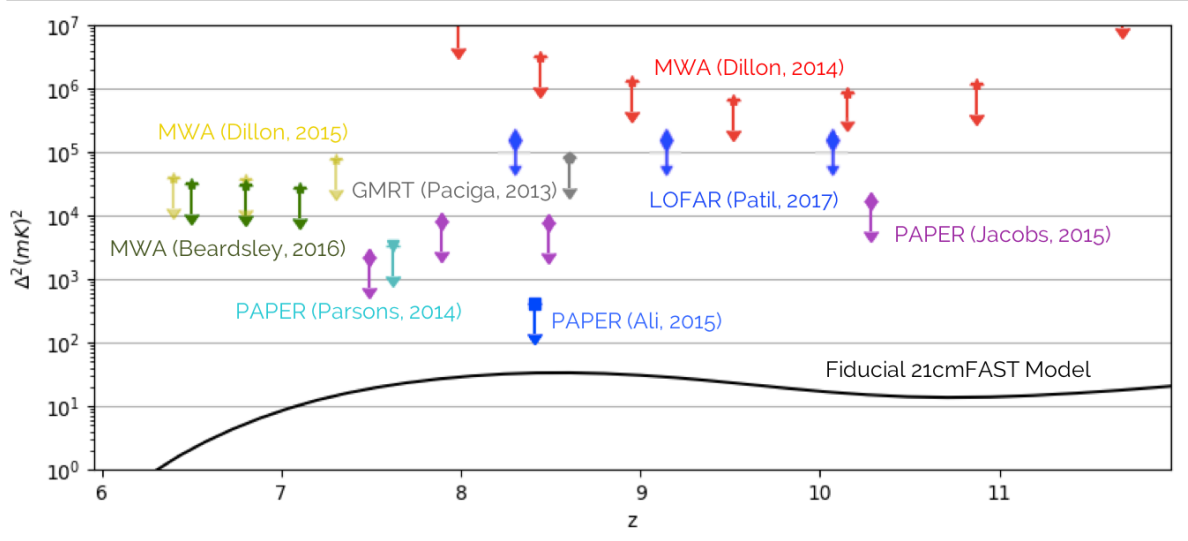


Figure 1.9: Published upper limits on the EoR placed by different 21 cm experiments, prior to the work in this thesis. All PAPER results shown (PAPER-32 is in cyan and magenta, and PAPER-64 is in blue) are suspect to the errors discussed throughout this work and are superseded by the ones presented in Chapter 3.

Related to the fundamental goal of simultaneously maximizing sensitivity and minimizing contaminants, some other challenges that face current 21 cm experiments include polarization leakage from Faraday-rotated emission (Moore et al. 2013; Kohn et al. 2016; Nunhokee et al. 2017), direction-dependent beam effects, and other low level sources of chromaticity induced by the instrument or calibration. These effects will require thorough investigations as experiments approach EoR sensitivities.

In addition to power spectrum experiments, there are several complementary experiments that aim to measure the sky-averaged global 21 cm signal (i.e., the mean brightness temperature of the EoR relative to the CMB). These include the Experiment to Detect the Global EoR Signature (EDGES; Bowman & Rogers 2010), the Large Aperture Experiment to Detect the Dark Ages (LEDA; Bernardi et al. 2016), the Dark Ages Radio Explorer (DARE; Burns et al. 2012), the Sonda Cosmológica de las Islas para la Detección de Hidrógeno NeutroSciHi (SCI-HI; Voytek et al. 2014), the Broadband Instrument for Global HydrOgen Reionisation Signal (BIGHORNS; Sokolowski et al. 2015), and the Shaped Antenna measurement of the background RAdio Spectrum (SARAS; Patra et al. 2015).

Like the power spectrum experiments, global signal experiments also face challenges of bright foregrounds and instrumental systematics. In particular, they require extremely precise calibration in order to avoid overfitting when subtracting foregrounds, and they also face additional challenges when observing the lowest frequencies, such as ionospheric fluctuations and brighter foregrounds (Vedantham et al. 2014; Datta et al. 2014).

However, most global signal telescopes consist of single elements and can therefore be more easily constructed. Additionally, EoR sensitivities can be reached with relatively short

observations. Thus, global signal experiments are actively being worked on as a complementary view into the evolution of the 21 cm signal. Accurate detections of the features of the global signal will delineate the different epochs in the early Universe, and their shapes will carry important implications about the nature of the IGM and the first sources.

For example, the first potential detection of the 21 cm signal has been made by the global signal experiment EDGES ([Bowman et al. 2018](#)). This exciting result suggests the presence of an absorption feature in the sky-averaged spectrum at 78 MHz, thought to be the result of the absorption of CMB photons by HI gas. Because the detected feature is best-fit by an amplitude much larger than what is consistent with expectations for the 21 cm signal during this epoch, alternate scientific explanations have been offered, such as the influence of dark matter on baryons and the effect of their interaction on the temperature of the gas ([Barkana 2018; Slatyer & Wu 2018](#)), . Measurements from other experiments in the future will certainly be informative in shaping the community’s confidence in this detection, and this result marks just the beginning of many more in the field to come.

Chapter 2

Power Spectrum Methods

- 2.1 Introduction to Themes
- 2.2 Signal Loss Toy Model
- 2.3 Signal Loss Mathematical Framework
- 2.4 Error Estimation Toy Model
- 2.5 Bias Toy Model

Chapter 3

PAPER-64

3.1 Overview

In the previous chapter we have discussed three overarching 21 cm power spectrum themes — signal loss, error estimation, and bias. Understanding the subtleties and trade-offs involved in each is necessary for an accurate and robust understanding of a power spectrum result.

We now apply these lessons to data from the PAPER experiment in order to illustrate our revised analysis pipeline. We begin with a brief overview of PAPER’s data processing steps prior to power spectrum estimation before delving into each theme in detail.

3.1.1 Observations

As described in Chapter 1.3.1, PAPER is a dedicated 21 cm experiment located in the Karoo Desert in South Africa. The PAPER-64 configuration consists of 64 dual-polarization drift-scan elements that are arranged in a grid layout (Figure 3.1). While every unique baseline is used for calibration, only a subset of the baselines are used for the power spectrum analysis in A15 (the three baselines used are the 30 m East/West baselines and their off-diagonal companions where two antennas are in adjacent columns and neighboring rows) and only one baseline-type is used for the demonstrations in this chapter (only the 30 m East/West baselines).

PAPER-64 conducted nighttime observations from November 2012 to March 2013. Over the course of the season, LST-coverage varied slightly, with power spectrum analyses focusing on the “cold patch” range from $\sim 0\text{--}8$ hours when the Galaxy is below the horizon. The PAPER correlator processes a 100–200 MHz bandwidth that consists of 1024 channels, each of width 97.6 kHz. Visibilities are integrated for 10.7 s before being written to disk.

PAPER’s raw data is compressed by a factor of ~ 70 through the use of RFI, delay, and delay-rate filters. More specifically, radio frequency interference is flagged at the 6σ level. Next, a low-pass delay filter is applied to all the data in order to filter out delays greater than the maximum delay allowed by the longest baseline in the array. Similarly, a low-pass

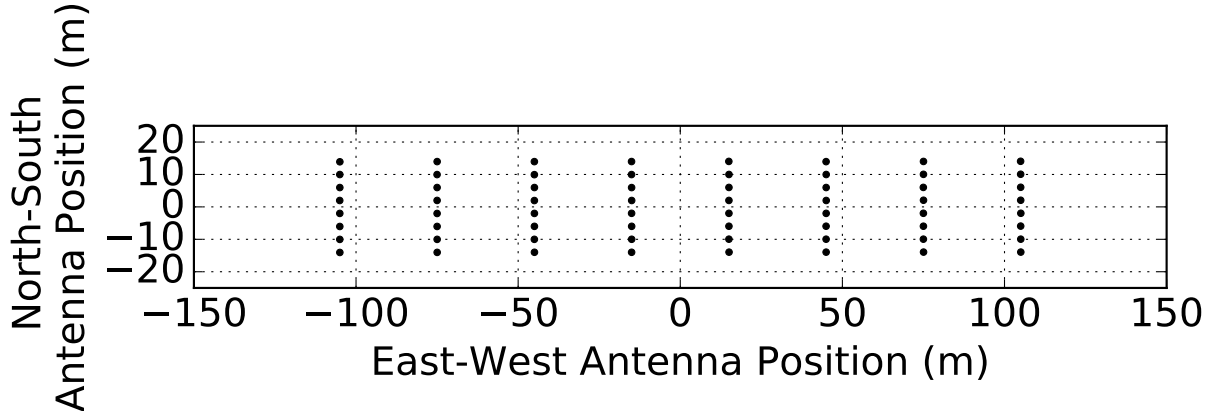


Figure 3.1: The PAPER-64 antenna layout. We use only 10 of the 30 m East/West baselines for the analysis in this paper (i.e., a subset of the shortest horizontal spacings).

fringe-rate, or delay-rate filter is applied to limit fringe-rates to allowable scales set by the array. Finally, the data is decimated to critical Nyquist sampling rates of 493 kHz and 42.9 s. For more details about PAPER’s data acquisition and compression pipelines, we refer the reader to [Parsons et al. \(2010\)](#) and [A15](#).

3.1.2 Data Processing

As described in Chapters [1.2.3](#), [1.2.4](#), [1.2.5](#), the primary post-processing steps of PAPER’s compressed data is calibration, foreground-filtering, and fringe-rate filtering. We now give a brief overview of each, as applied to PAPER data.

We employ the package OMNICAL for redundant calibration ([Zheng et al. 2014](#)), which comprises of three steps. The first is `FirstCal`, which uses all baseline redundancies to generate a static gain solution for each antenna that will unwrap any phase wrapping between two identical baselines. We perform `FirstCal` because the next stage of OMNICAL cannot tell the difference between a phase of 0 and 2π , for example. The second step is `LogCal`, which takes the log of all the visibility equations (Equation [\(1.8\)](#)) and separates the real and imaginary components into two matrices. Coarse solutions are determined for both the antenna gains and “model” visibilities (one for each baseline type) simultaneously. The final step of OMNICAL is `LinCal`, which applies small perturbations to the `LogCal` solutions in an iterative fashion, honing in on the optimal solutions.

It is important to note that while OMNICAL is powerful for ensuring array redundancy, it is not able to solve for 4 calibration parameters - namely, the overall gain, phase, and tip/tilt of the array. For absolute calibration, we turn to a standard self-calibration routine which includes imaging Pictor A, Fornax A, and the Crab Nebula in order to fit for the overall phase solutions and the flux scale.

After calibration, we combine the XX and YY linear polarization data to form pseudo-

Stokes I as defined as:

$$V_I = \frac{1}{2}(V_{XX} + V_{YY}) \quad (3.1)$$

(Moore et al. 2013).

Next, a delay-filter is used to filter out foregrounds contained inside the maximum delay set by each baseline. This is accomplished by de-convolving out our sampling function (which contains flags due to RFI) from our delay-domain visibilities using a CLEAN-like algorithm that restricts our clean components to inside the horizon limit, plus a 15 ns buffer. The Fourier-transformed clean components are then subtracted from our visibilities. This filtering process is performed on a per-baseline, per-integration basis, and we achieve a brightness suppression of ~ 4 orders of magnitude in our visibilities.

After delay-filtering, we perform a final round of RFI-removal by flagging visibilities that lie more than 3σ above the mean on a time, frequency, and baseline basis. Finally, we stack our data in LST into two datasets, alternating between even and odd Julian Dates to create an “even” and “odd” LST-binned dataset. A total of 124 days of data are included in the LST-binned dataset.

The final step before power spectrum estimation is fringe-rate filtering. The chosen filter (which is described in the next section) is applied on a per-baseline basis and weights the fringe-rate bins on the sky by the RMS of the primary beam at that same location. A smooth filter is constructed by fitting a Gaussian to the filter shape in the fringe-rate domain. Additionally, fringe-rates below 0.2 mHz are zeroed out, effectively removing slowly-varying signals such as crosstalk. We then convolve our time-domain visibilities by the Fourier-transform of the fringe-rate filter to yield time-averaged visibilities that have gained another order of magnitude in sensitivity.

3.1.3 Case Study Data

For the case study presented in the rest of this chapter, we focus on a subset of the PAPER-64 data used in A15, namely, on LST-binned, Stokes I estimated data (Moore et al. 2013) from PAPER’s 30 m East/West baselines (Figure 3.1). Hence, all data processing steps are identical to those in A15 until after the LST-binning step in Figure 3 of A15.

The previously best published 21 cm upper limit result from A15 placed a 2σ upper limit on $\Delta^2(k)$, defined as

$$\Delta^2(k) = \frac{k^3}{2\pi^2} \hat{P}(k), \quad (3.2)$$

of $(22.4 \text{ mK})^2$ in the range $0.15 < k < 0.5 h \text{ Mpc}^{-1}$ at $z = 8.4$. The need to revise this limit stems mostly from previously under-estimated signal loss and under-estimated error bars, both of which we address in the following sections.

For the analysis in this paper, we use 8.1 hours of LST, namely an RA range of 0.5-8.6 hours (A15 uses a slightly longer RA range of 0-8.6 hours; we found that some early LSTs

were more severely foreground contaminated). We also use only 10 baselines, a subset of the 51 total East/West baselines used in A15, in order to illustrate our revised methods. All power spectrum results are produced for a center frequency of 151 MHz using a width of 10 MHz (20 channels), identical to the analysis in A15. In the case study in this paper, we only use one baseline type instead of the three as in A15, but Kolopanis et al. (*in prep.*) uses the full dataset presented in A15 to revise the result and place limits on the EoR at multiple redshifts (using a straightforward and not lossy approach to avoid many of the issues presented in this paper).

The most significant changes from A15 occur in our revised power spectrum analysis, which is explained in the rest of this paper, but we also note that the applied fringe-rate filter is also slightly different. In A15, the applied filter was not equivalent to the optimal fringe-rate filter (which is designed to maximize power spectrum sensitivity). Instead, the optimal filter was degraded slightly by widening it in fringe-rate space. This was chosen in order to increase the number of independent modes and reduce signal loss associated with the quadratic estimator, though as we will explain in the next section, this signal loss was still under-estimated. With the development of a new, robust method for assessing signal loss, we choose to use the optimal filter in order to maximize sensitivity. This filter is computed for a fiducial 30 m baseline at 150 MHz, the center frequency in our band. The filter in both the fringe-rate domain and time domain is shown in Figure 3.2.

Finally, we emphasize that the discussion that follows is solely focused on signal loss associated with empirical covariance weighting. As mentioned in Chapter ??, there are several other ways the PAPER analysis pipeline can lead to loss, including through calibration and delay-filtering. We refer the reader to Parsons et al. (2010) and A15 for discussions about these other types of signal loss, noting here that they are much less significant than the loss focused on in this paper.

3.2 Signal Loss

3.3 Error Estimation

3.4 Bias

3.5 Power Spectrum Limits

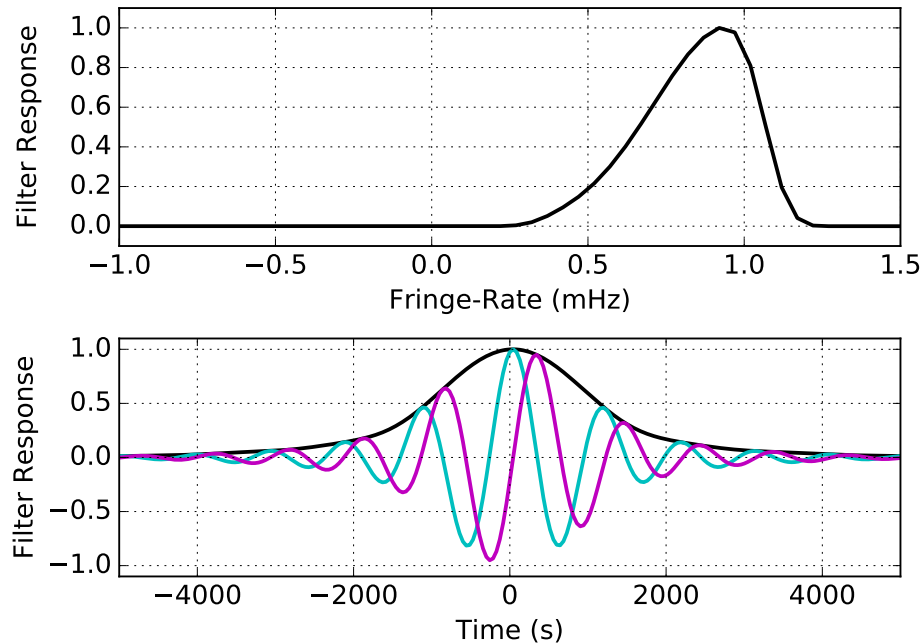


Figure 3.2: Top: the normalized optimal power-spectrum sensitivity weighting in fringe-rate space for our fiducial baseline and Stokes I polarization beam. Bottom: the time domain convolution kernel corresponding to the top panel. Real and imaginary components are illustrated in cyan and magenta, respectively, with the absolute amplitude in black. The fringe-rate filter acts as an integration in time, increasing sensitivity but reducing the number of independent samples in the dataset.

Chapter 4

PAPER-128

4.1 Overview

The PAPER experiment expanded out to 128 antennas in 2013 and observed for two seasons. The first season began in November, 2013 and lasted until March, 2014. The second began in July, 2014 and ended in January, 2015. The PAPER-128 configuration consists of 112 core antennas arranged in a grid layout (7 rows and 16 columns), with neighboring East/West spacings being 15 m and neighboring North/South spacings being 4 m (Figure 4.1). Additionally, 16 outrigger antennas were placed in strategic locations in order to form long baselines and increase *uv*-plane sampling. These outrigger antennas are not used for the power spectrum analysis presented in this thesis, but are useful for imaging analyses.

In general, the signal chain of PAPER-128 is similar to that of PAPER-64. However, one major change is the addition of receiverators on site, which houses the receivers used to amplify and filter the antenna signals. Prior to this change, the receivers were located inside a cooled shipping container along with the rest of the DSP system. With the addition of more antennas, however, the receivers were moved outside the container to save space.

Although PAPER-128 doubled in the number of antennas, the data collected by this array is typically found to be lower in quality than that of PAPER-64. There are many reasons for this, including general wear and tear on the instrument and the addition of the receiverators (which had no monitoring system and, as we will see, is one of the main reasons for missing and corrupted PAPER-128 data). Because of these issues, PAPER-128 requires the development of novel techniques in order to filter out contaminated data products prior to analysis. Using the entire season of data, without any filtering, would result in a power spectrum analysis severely dominated by systematics and (non-EoR) detections. Thus, one of the unique challenges facing PAPER-128 is how to automatically and accurately detect and remove bad data (i.e., misbehaving baselines, dead receiverators, criss-crossed signal paths, etc.) in order to curate a dataset as free of systematics as possible.

In this chapter, we present methods developed for the detection of corrupt data in PAPER-128. These methods represent the first routinely-used “quality assurance” steps for the PAPER experiment. They also represent the first generation of data assessment

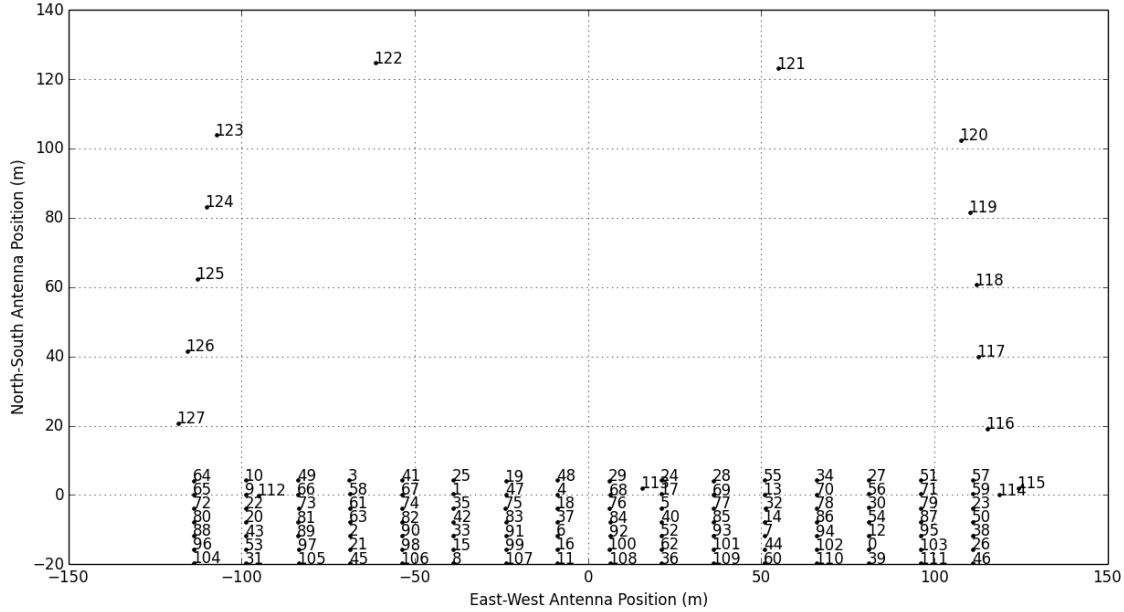


Figure 4.1: The PAPER-128 antenna layout. There are 112 antennas arranged in a grid layout which are used for power spectrum analyses. The addition of 16 outrigger antennas is used to increase *uv*-plane sampling for imaging analyses.

techniques that are currently being expanded upon for incorporation into HERA’s real-time processing system.

Additionally in this chapter, we process two epochs of PAPER-128 data (both from the first season) and show power spectrum results for each. We do not show results from the second season of data due to increased hardware failure that was experienced at the end of PAPER-128’s deployment. As such, the first season of PAPER-128 represents the bulk of the array’s sensitivity (though we note that the limits do not surpass those of PAPER-64, mostly due to having fewer days of data). Table ?? gives an overview of the PAPER-128 dataset analyzed in this thesis.

4.2 Quality Assurance

Post-processing of PAPER data relies heavily on the array’s redundancy, and any sources of non-redundancy have the potential to corrupt redundant calibration and power spectrum estimation. These sources of error — which span from the failure of analog or digital components to improper feed installation to the accidental deletion and subsequent recovery of data products — manifest themselves in corrupted data that can be found primarily along two main axes: the time-axis and the antenna-axis.

We next present metrics that we have developed to locate contaminated data along

Epoch	Dates	Number of Days Analyzed	Flagged Days	Flagged Antennas
1	Nov 2013 - Jan 2014 JDs 6617-6673	38	6647,6662,6664, 6665,6673	3,7,8,16,19,20, 27,28,34,53, 56,84,85,96,100 FX2: 2,10,15,22,31, 33,42,43,47,58, 64,72,91,97,105,107
2	Jan 2014 - March 2014 JDs 6678-6724	40	6692,6702,6704, 6706,6717,6730	3,7,16,27,34,56, 57,84,85,100,110

Table 4.1: An overview of the PAPER-128 data used for power spectrum analysis in this thesis.

these axes. We use the results of these metrics to remove specific days of data and specific antennas from our analysis prior to calibration in order to ensure robust calibration that is not influenced by outlier data.

4.2.1 Flagging Julian Dates

To better assess the variation of PAPER-128 data across its two-year deployment (which consists of 7+ individual epochs of data, where an epoch is characterized by the shut-down and re-starting of the correlator), we first investigate one-dimensional slices of compressed data that span the entire time axis but only one frequency channel. We choose channel 100 for this analysis, as its corresponding frequency of 1.5 GHz lies in the middle of our band (similar to PAPER-64, PAPER-128’s bandwidth consists of 203 frequency channels ranging from 100 to 200 MHz).

We look at the visibility amplitude of each day of data in an epoch as a function of LST, shown as the different colors in Figure 4.2. We designate a reference day to each epoch (a manually chosen “good” day), and flag days that differ from the reference day by more than 20%. After flagging, visibilities show good day-to-day agreement across an epoch (bottom row of Figure 4.2).

An example of data from a particularly “bad” day is shown in Figure 4.3. It is clear that Julian date 2456692 differs dramatically from reference day 2456680, as it contains many corrupted files throughout the day due to failure somewhere in the signal chain. This failure mode is often due to the accidental deletion and erroneous recovery of data (much of the season’s data was accidentally deleted prior to any of the work in this thesis), as well as hardware failures (e.g., loose cable connections) that result in lost sky fringes. From Table ??, we see that a total of 38 days pass our flagging metric for Epoch 1 and 40 days pass for Epoch 2 (both from PAPER-128’s first observing season), and a total of five and six days are flagged for each epoch, respectively.

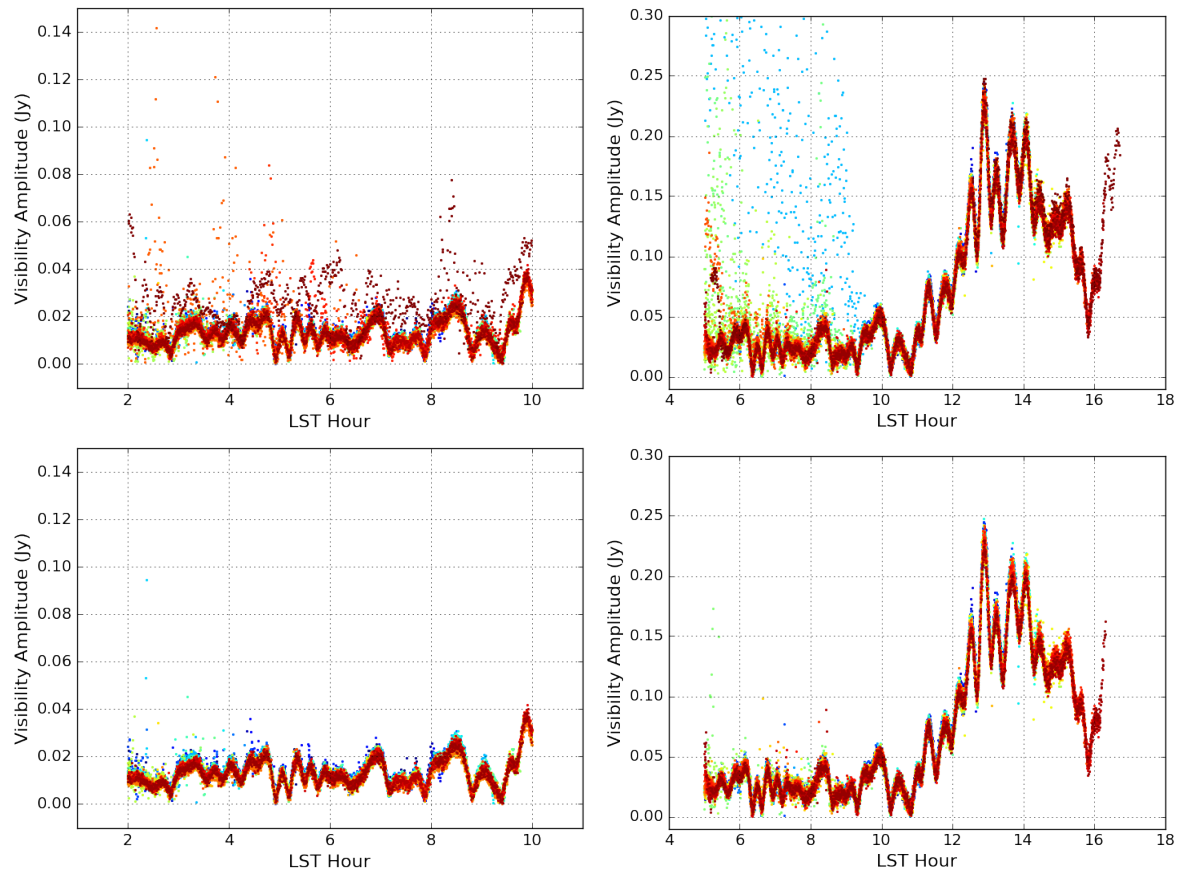


Figure 4.2: Visibility amplitudes as a function of LST for different Julian days of data. The left column shows the data before (top) and after (bottom) the flagging of outlier days for Epoch 1. The right column shows similar data for Epoch 2.

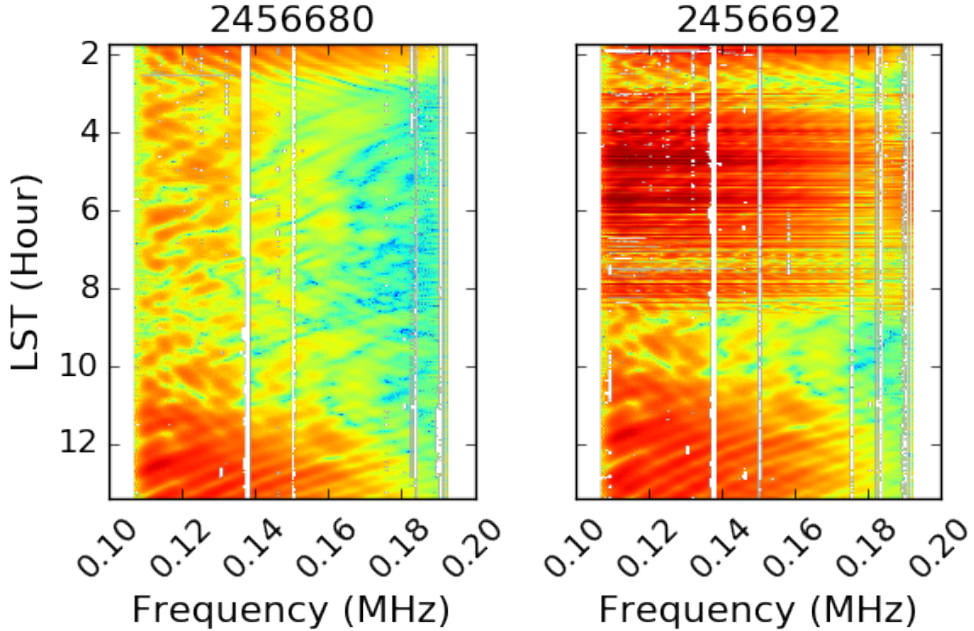


Figure 4.3: Waterfall plots of visibility amplitudes for a “good” reference day (left) in Epoch 2 and “bad” day (right). We exclude corrupted data for specific days found with our metric.

4.2.2 Flagging Antennas

There are a few types of failure modes for data associated with specific antennae. The first is if feeds are accidentally rotated by 90 degrees (or equivalently, the cables for the XX and YY polarizations are swapped). Consequently, visibilities involving a “cross-polarized” antenna exhibit visibility amplitudes that are more weakly correlated (lower amplitude) than what is expected for an XX or YY visibility (and similarly, XY and YX visibilities exhibit too high of an amplitude). In order to locate potentially cross-polarized antennae, we use the following metric:

$$M_i = \frac{\sum_{j,\nu,t} |V_{ij}|}{(N-1)}, \quad (4.1)$$

where the visibility for baseline ij is summed for every j^{th} antenna, frequency ν , and time t , and N is the number of antennas. We compute this metric for all four polarizations (XX, XY, YX, YY). Next, for each night of data we form the polarization fraction quantity:

$$P_i = \frac{M_i^{XY} + M_i^{YX}}{M_i^{XX} + M_i^{YY}}. \quad (4.2)$$

We expect the numerator of this quantity to be higher than the denominator for cross-polarized antennae. In practice, we form polarization fractions for every antenna and flag

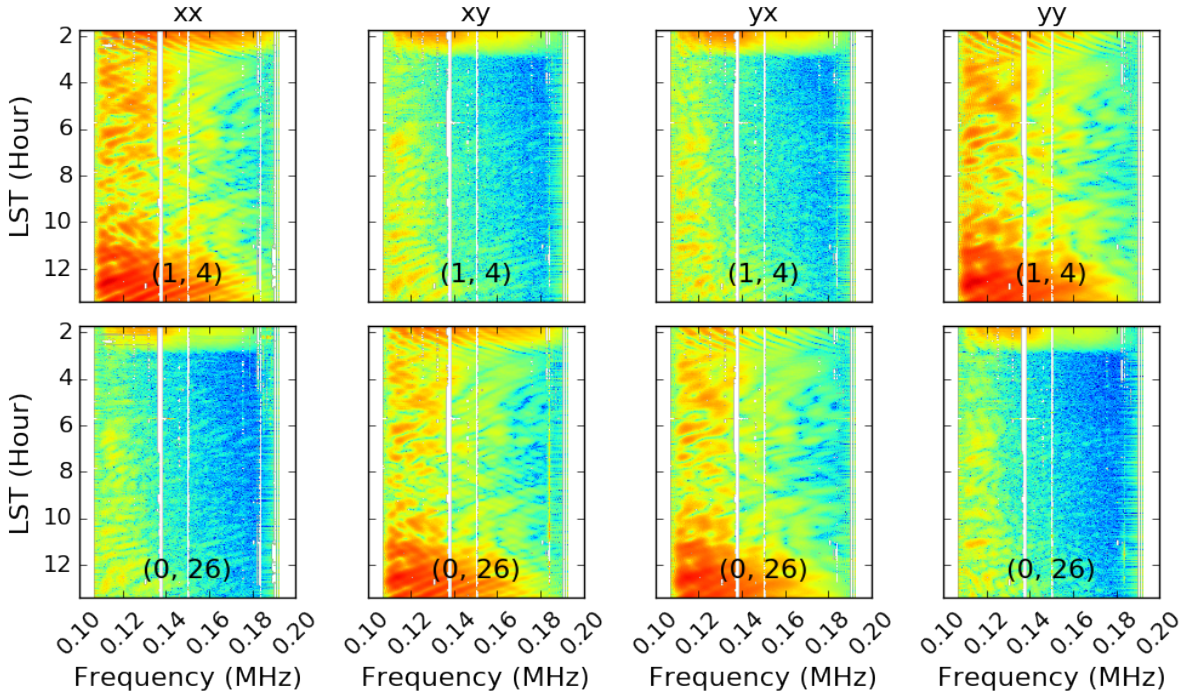


Figure 4.4: Waterfall plots of visibility amplitudes for four different polarizations and two different baselines. Antenna 26 is found to be cross-polarized because its feed was rotated by 90 degrees, and hence its “X” and “Y” polarization states are mis-labeled. Equation (4.2) captures visibility amplitudes like the ones shown here in order to automatically detect cross-polarized antennae.

those with high P_i values as being cross-polarized. We note that this metric works best for long baselines, where XX and XY visibilities are expected to have different signal-to-noise over short distance scales. For short baselines (and large-scales), astrophysical polarization has been shown to be present in all polarization quantities, including the linear ones, thus bringing P_i closer to unity (Lenc et al. 2016).

Using this metric, we find six antennas to be cross-polarized in PAPER-128 observations (antennas 26, 34, 38, 46, 50, and 72). An example of visibilities containing antenna 26 is shown in Figure 4.4, and it is clear that the “X” and “Y” polarizations are swapped for baselines involving that antenna. We fix this issue, re-naming polarization states where necessary, for all the compressed PAPER-128 data before performing other quality assessment tests and calibration.

Another failure mode is an antenna that exhibits low amplitude, a fairly common occurrence as different electronic components can cause the temporary reduction or loss of power. A drastic example of this is when an entire correlator (FX2) was accidentally shut-off, cutting off connections to 16 antennas. The loss of those 16 antennas only affected Epoch 1, and the correlator was then re-started for Epoch 2.

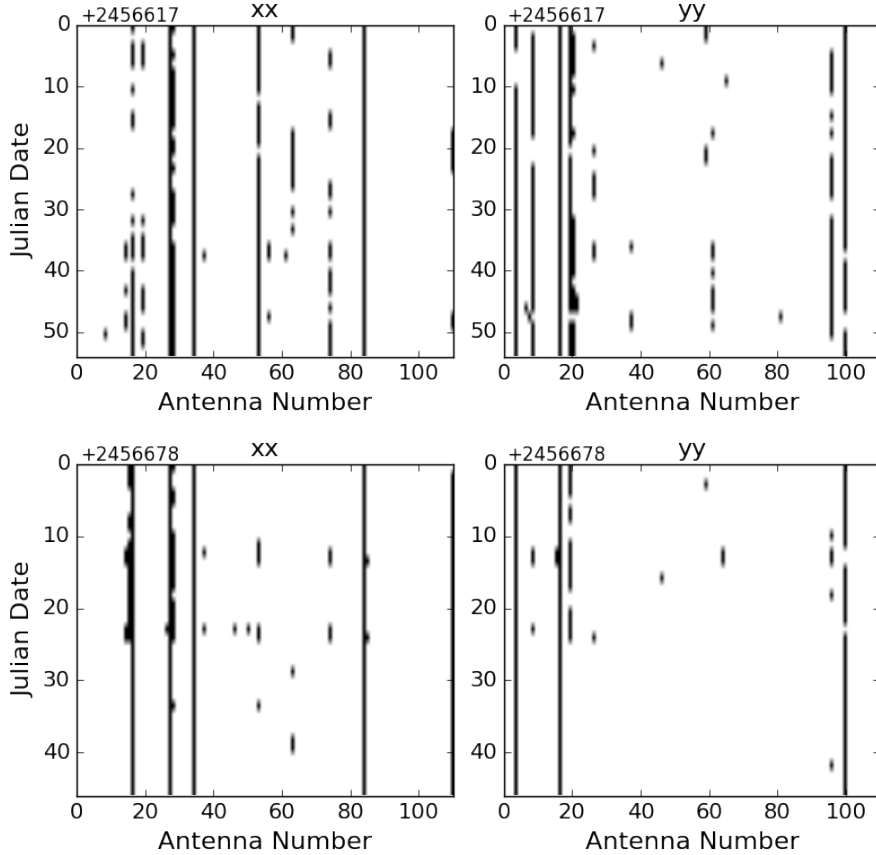


Figure 4.5: Flagged antennas, found using Equation (4.1), are marked in black for each antenna number (x-axis) and Julian date (y-axis). The left column shows flags for XX polarization, and the right column shows flags for YY polarization. The top row shows flags for Epoch 1 and the bottom row shows flags for Epoch 2. We remove antennas that are flagged greater than 50% of the time per epoch.

In order to find antennas with unusually low signals, we again employ Equation (4.1), computing the metric for every antenna. Comparing M_i across the entire array can reveal which antennas are consistently misbehaving. We then flag antennas with M_i values that are low by at least 1σ . Figure 4.5 shows these antenna flags across both epochs, and we remove all data associated with antennas that are flagged greater than 50% of the time (for each epoch, we combine the flags for the XX and YY polarizations).

Almost all of the flagged antennas listed in Table ?? are found via the metric described above. However, we do note that a couple were found manually by visually inspecting visibility data and `Omnical` results. While our metric does a good job locating antennas with low amplitudes, we found that there were certain antennas (usually one-off instances) with additional issues that do not fall under any of our previous metrics and would require a more sophisticated metric to be able to find automatically.

Finally, we highlight the importance of flagging antennas prior to redundant calibration by showing `FirstCal` phase solutions for a single antenna without flagging and with flagging (Figure 4.6, top). `Omnical` χ^2 results are also shown (bottom). These results depict how the quality of redundant calibration (the stability of the calibration solutions and level of redundancy) depends on the behavior of the antennas. It is evident that the `FirstCal` solutions are unstable from file to file without any initial antenna flagging (top left). Similarly, higher χ^2 values means that the `Omnical` model visibilities differ substantially from the gain-corrected measured visibilities, meaning redundant calibration is poor. It is obvious that pre-calibration flagging metrics are crucial in order to robustly calibrate PAPER-128 data.

4.3 Data Processing

We process both epochs of PAPER-128 data, closely following the PAPER-64 processing steps outlined in Chapter 3.1.2. One specific difference from the PAPER-64 pipeline is that we aggressively flag RFI prior to delay-filtering in order to prevent low levels of spectral structure from leaking into the EoR window. Because the overall quality of PAPER-128 data is in general lower than PAPER-64, we found that aggressive flagging methods are worthwhile in order to maximize signal-to-noise. To accomplish this, we first flag calibrated visibilities on a per-frequency, per-integration basis based on OMNICAL χ^2 values (using a 6σ deviation cutoff). This masks potentially problematic data identified from the redundant calibration solutions. In addition, we manually flag ten known channels of RFI.

Delay-filtering proceeds identically to the PAPER-64 pipeline. We then bin both the foreground-containing and foreground-removed data by LST into separate datasets. For both these datasets, we form Stokes I.

Recalling that redundant calibration only solves for internal calibration parameters, absolute calibration remains needed. In the PAPER-64 analysis, a self-calibration method was used to solve for overall gain and phase calibration solutions (immediately after redundant calibration). Trusting these solutions, we can then calibrate the PAPER-128 data to the calibrated PAPER-64 data. To do this, we use foreground-containing, LST-binned data for both PAPER-64 and PAPER-128 (where the PAPER-64 dataset is calibrated) and look at a matching fiducial baseline for each. We align both datasets in LST and compute the ratio of the two for every time integration and frequency channel. We then average these ratios over time to yield a bandpass solution.

Mathematically, if the visibility data for PAPER-64 and PAPER-128 are written as the following complex numbers:

$$V_{64} = ae^{i\phi_a} \quad (4.3)$$

$$V_{128} = be^{i\phi_b}, \quad (4.4)$$

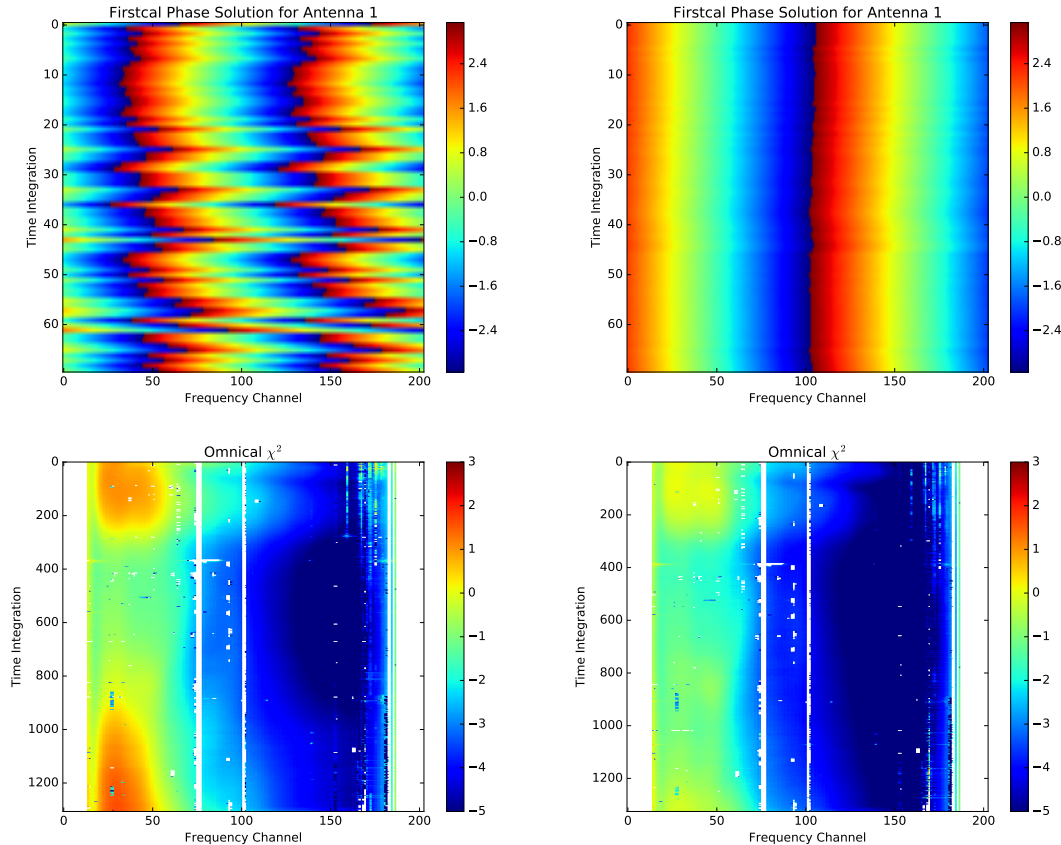


Figure 4.6: FirstCal phase solutions for Antenna 1 (Epoch 1, XX polarization) where no antennas are flagged (top left) and some antennas are flagged (via the methods described in Chapter 4.2.2, top right). Omnical χ^2 results are also shown for the two cases (bottom). We do not include any of the dead 16 antennas associated with correlator FX2. It is crucial to flag misbehaving antennas (especially extreme outlier antennas) prior to redundant calibration, motivating the development of automated quality assessment tools prior to the post-processing of data.

then we solve for an overall gain correction factor as:

$$f_{gain} = \frac{a}{b} \quad (4.5)$$

and an overall phase factor as:

$$f_\phi = \phi_a - \phi_b. \quad (4.6)$$

Combining these two gives the bandpass solution (one number per frequency):

$$f = f_{gain} e^{if_\phi}. \quad (4.7)$$

Using this bandpass, we fit an eighth order polynomial to smooth the solutions and apply this multiplicative factor to the delay-filtered, LST-binned PAPER-64 data. We calibrate each epoch of data separately. We note that this coarse absolute calibration is only a rough calibration, and a more careful, sky-based calibration is recommended for precise results. However, using this simple calibration yields foreground data that agrees with the PAPER-64 data to within $\sim 20\%$.

Finally, the last step of processing is fringe-rate filtering, where an optimal filter is used to combine the data and filter out excess noise. PAPER-128 has an original integration time of 32 s, making the optimal filter length to be ~ 3910 s, slightly longer than that of PAPER-64.

4.4 Power Spectrum Limits

We form power spectrum estimates for both epochs of data and two frequency channel ranges: 139-149 MHz ($z=8.9$) and 154-164 MHz ($z=7.9$). Both bands consist of 21 channels (each 0.5 MHz) and are relatively absent of RFI. We focus only on one baseline-separation type, namely all 30 m East/West baselines (of which there are 51 in the first epoch of 79 in the second). Our power spectrum formalism follows the analysis outlined in Chapter 3 and uses all updated methods regarding bootstrapping and noise sensitivity estimation. Because empirical inverse covariance weighting is shown to be extremely lossy for fringe-rate filtered PAPER data (Chapter ??) and regularization techniques do not significantly improve power spectrum sensitivity (Chapter ??), we form unweighted limits ($\mathbf{C} \equiv \mathbf{I}$) in an effort to present straightforward, reliable results.

Figure 4.7 shows the power spectrum results for PAPER-128. The two epochs are displayed as columns and the two redshifts as rows. Black and gray data points represent positive and negative power spectrum values, respectively (calculated as the average power spectrum value over all baseline pairs), and they have 2σ error bars that are calculated from bootstrapping over baselines. The solid green curve is our theoretical prediction of our sensitivity, computed analytically using Equation (??). This sensitivity prediction is also plotted as gray shaded regions around the data points.

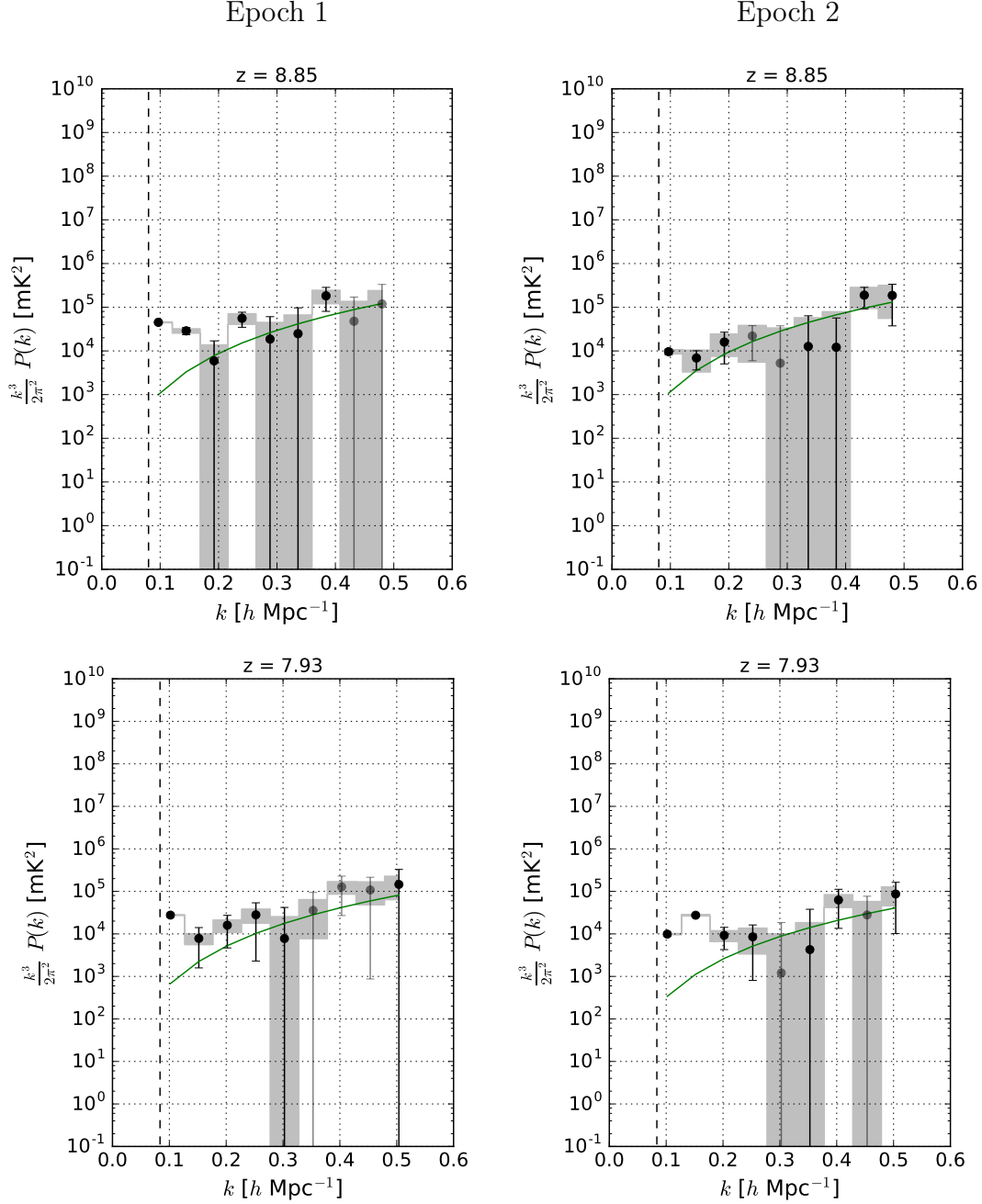


Figure 4.7: Power spectrum results for PAPER-128 season 1 data for two redshifts (rows) and two epochs (columns), using one baseline separation-type only (30 m East/West baselines). Black and gray points represent positive and negative power spectrum values, respectively, with 2σ error bars determined from bootstrapping. The 2σ theoretical noise sensitivity prediction is shown in green. Gray shaded regions correspond to theoretical errors on each data point.

Chapter 5

HERA

Chapter 6

Conclusion

Bibliography

- Ali, Z. S., Parsons, A. R., Zheng, H., et al. 2015, *ApJ*, 809, 61
- Barkana, R. 2009, *Monthly Notices of the Royal Astronomical Society*, 397, 1454
- . 2018, *Nature*, 555, 71
- Barkana, R., & Loeb, A. 2008, *Monthly Notices of the Royal Astronomical Society*, 384, 1069
- Beardsley, A. P., Hazelton, B. J., Sullivan, I. S., et al. 2016, *The Astrophysical Journal*, 833, 102
- Becker, R. H., Fan, X., White, R. L., et al. 2001, *AJ*, 122, 2850
- Bernardi, G., Zwart, J. T. L., Price, D., et al. 2016, *MNRAS*, 461, 2847
- Bowman, J. D., Morales, M. F., & Hewitt, J. N. 2009, *The Astrophysical Journal*, 695, 183
- Bowman, J. D., & Rogers, A. E. E. 2010, *Nature*, 468, 796
- Bowman, J. D., Rogers, A. E. E., Monsalve, R. A., Mozdzen, T. J., & Mahesh, N. 2018, *Nature*, 555, 67
- Burns, J. O., Lazio, J., Bale, S., et al. 2012, *Advances in Space Research*, 49, 433
- Chapman, E., Zaroubi, S., Abdalla, F. B., et al. 2016, *Monthly Notices of the Royal Astronomical Society*, 458, 2928
- Datta, A., Bowman, J. D., & Carilli, C. L. 2010, *The Astrophysical Journal*, 724, 526
- Datta, K. K., Jensen, H., Majumdar, S., et al. 2014, *MNRAS*, 442, 1491
- DeBoer, D. R., Parsons, A. R., Aguirre, J. E., et al. 2017, *Publications of the Astronomical Society of the Pacific*, 129, 045001
- Dillon, J. S., & Parsons, A. R. 2016, *The Astrophysical Journal*, 826, 181
- Dillon, J. S., Liu, A., Williams, C. L., et al. 2014, *Phys. Rev. D*, 89, 023002
- Dillon, J. S., Neben, A. R., Hewitt, J. N., et al. 2015a, *Phys. Rev. D*, 91, 123011
- Dillon, J. S., Tegmark, M., Liu, A., et al. 2015b, *Phys. Rev. D*, 91, 023002
- Dodelson, S. 2003, Modern cosmology (San Diego, CA: Academic Press)
- Ewall-Wice, A., Dillon, J. S., Liu, A., & Hewitt, J. 2017, *MNRAS*, 470, 1849
- Fialkov, A., Barkana, R., Pinhas, A., & Visbal, E. 2014, *Monthly Notices of the Royal Astronomical Society: Letters*, 437, L36
- Fialkov, A., Barkana, R., & Visbal, E. 2014, *Nature*, 506, 197
- Furlanetto, S. R., Oh, S. P., & Briggs, F. H. 2006, *Phys. Rep.*, 433, 181
- Haiman, Z., & Knox, L. 1999, in *Astronomical Society of the Pacific Conference Series*, Vol. 181, Microwave Foregrounds, ed. A. de Oliveira-Costa & M. Tegmark, 227
- Harker, G., Zaroubi, S., Bernardi, G., et al. 2009, *Monthly Notices of the Royal Astronomical Society*, 397, 1454

- Society, 397, 1138
- Hazelton, B. J., Morales, M. F., & Sullivan, I. S. 2013, *The Astrophysical Journal*, 770, 156
- Hinshaw, G., Larson, D., Komatsu, E., et al. 2013, *ApJS*, 208, 19
- Jacobs, D. C., Pober, J. C., Parsons, A. R., et al. 2015, *ApJ*, 801, 51
- Jacobs, D. C., Hazelton, B. J., Trott, C. M., et al. 2016, *ApJ*, 825, 114
- Jelić, V., Zaroubi, S., Labropoulos, P., et al. 2008, *MNRAS*, 389, 1319
- Kohn, S. A., Aguirre, J. E., Nunhokee, C. D., et al. 2016, *ApJ*, 823, 88
- Koopmans, L., Pritchard, J., Mellema, G., et al. 2015, Advancing Astrophysics with the Square Kilometre Array (AASKA14), 1
- Lenc, E., Gaensler, B. M., Sun, X. H., et al. 2016, *The Astrophysical Journal*, 830, 38
- Liu, A., Parsons, A. R., & Trott, C. M. 2014a, *Phys. Rev. D*, 90, 023018
- . 2014b, *Phys. Rev. D*, 90, 023019
- Liu, A., Tegmark, M., Bowman, J., Hewitt, J., & Zaldarriaga, M. 2009, *Monthly Notices of the Royal Astronomical Society*, 398, 401
- Liu, A., Tegmark, M., Morrison, S., Lutomirski, A., & Zaldarriaga, M. 2010, *Monthly Notices of the Royal Astronomical Society*, 408, 1029
- Loeb, A., & Furlanetto, S. 2013, The First Galaxies in the Universe (Princeton University Press)
- Lonsdale, C., J. Cappallo, R., F. Morales, M., et al. 2009, Proceedings of the IEEE, 97, 1497
- Moore, D. F., Aguirre, J. E., Parsons, A. R., Jacobs, D. C., & Pober, J. C. 2013, *The Astrophysical Journal*, 769, 154
- Morales, M. F., Bowman, J. D., & Hewitt, J. N. 2006, *The Astrophysical Journal*, 648, 767
- Morales, M. F., & Wyithe, J. S. B. 2010, *ARA&A*, 48, 127
- Neben, A. R., Bradley, R. F., Hewitt, J. N., et al. 2016, *The Astrophysical Journal*, 826, 199
- Nunhokee, C. D., Bernardi, G., Kohn, S. A., et al. 2017, *The Astrophysical Journal*, 848, 47
- Offringa, A. R., de Bruyn, A. G., & Zaroubi, S. 2012, *Monthly Notices of the Royal Astronomical Society*, 422, 563
- Paciga, G., Albert, J. G., Bandura, K., et al. 2013, *MNRAS*, arXiv:1301.5906 [astro-ph.CO]
- Parsons, A., Pober, J., McQuinn, M., Jacobs, D., & Aguirre, J. 2012, *ApJ*, 753, 81
- Parsons, A. R., & Backer, D. C. 2009, *The Astronomical Journal*, 138, 219
- Parsons, A. R., Liu, A., Ali, Z. S., & Cheng, C. 2016, *ApJ*, 820, 51
- Parsons, A. R., Pober, J. C., Aguirre, J. E., et al. 2012, *The Astrophysical Journal*, 756, 165
- Parsons, A. R., Backer, D. C., Foster, G. S., et al. 2010, *AJ*, 139, 1468
- Parsons, A. R., Liu, A., Aguirre, J. E., et al. 2014, *ApJ*, 788, 106
- Patil, A. H., Yatawatta, S., Koopmans, L. V. E., et al. 2017, *ApJ*, 838, 65
- Patra, N., Subrahmanyam, R., Sethi, S., Udaya Shankar, N., & Raghunathan, A. 2015, *ApJ*, 801, 138
- Patra, N., Parsons, A. R., DeBoer, D. R., et al. 2018, *Experimental Astronomy*, 45, 177
- Peterson, U.-L. P. X.-P. W. J. 2004, ArXiv Astrophysics e-prints, astro-ph/0404083
- Planck Collaboration, Ade, P. A. R., Aghanim, N., et al. 2016, *A&A*, 594, A13
- Pober, J. C., Parsons, A. R., Jacobs, D. C., et al. 2012, *AJ*, 143, 53
- Pober, J. C., Parsons, A. R., Aguirre, J. E., et al. 2013, *The Astrophysical Journal Letters*,

- 768, L36
- Pober, J. C., Liu, A., Dillon, J. S., et al. 2014, *ApJ*, 782, 66
- Pober, J. C., Ali, Z. S., Parsons, A. R., et al. 2015, *ApJ*, 809, 62
- Pritchard, J. R., & Loeb, A. 2010, *Phys. Rev. D*, 82, 023006
- . 2012, *Reports on Progress in Physics*, 75, 086901
- Robertson, B. E., Ellis, R. S., Furlanetto, S. R., & Dunlop, J. S. 2015, *ApJ*, 802, L19
- Roshi, D. A., & Perley, R. A. 2003, in Astronomical Society of the Pacific Conference Series, Vol. 306, New technologies in VLBI, ed. Y. C. Minh, 109
- Santos, M. G., Cooray, A., & Knox, L. 2005, *ApJ*, 625, 575
- Slatyer, T. R., & Wu, C.-L. 2018, *Phys. Rev. D*, 98, 023013
- Sokolowski, M., Tremblay, S. E., Wayth, R. B., et al. 2015, *PASA*, 32, e004
- Sullivan, I. S., Morales, M. F., Hazelton, B. J., et al. 2012, *The Astrophysical Journal*, 759, 17
- Thompson, A. R., Moran, J. M., & Swenson, Jr., G. W. 2001, *Interferometry and Synthesis in Radio Astronomy*, 2nd Edition (Springer)
- Thyagarajan, N., Jacobs, D. C., Bowman, J. D., et al. 2015, *The Astrophysical Journal*, 804, 14
- Tingay, S. J., Goeke, R., Bowman, J. D., et al. 2013, *PASA*, 30, 7
- Trott, C. M., Wayth, R. B., & Tingay, S. J. 2012, *ApJ*, 757, 101
- Trott, C. M., Pindor, B., Procopio, P., et al. 2016, *The Astrophysical Journal*, 818, 139
- van Haarlem, M. P., Wise, M. W., Gunst, A. W., et al. 2013, *A&A*, 556, A2
- Vedantham, H., Shankar, N. U., & Subrahmanyan, R. 2012, *The Astrophysical Journal*, 745, 176
- Vedantham, H. K., Koopmans, L. V. E., de Bruyn, A. G., et al. 2014, *MNRAS*, 437, 1056
- Voytek, T. C., Natarajan, A., Jáuregui García, J. M., Peterson, J. B., & López-Cruz, O. 2014, *ApJ*, 782, L9
- Wang, X., Tegmark, M., Santos, M. G., & Knox, L. 2006, *ApJ*, 650, 529
- Weisz, D. R., & Boylan-Kolchin, M. 2017, *MNRAS*, 469, L83
- Wu, X. 2009, in Bulletin of the American Astronomical Society, Vol. 41, American Astronomical Society Meeting Abstracts #213, 474
- Zheng, H., Tegmark, M., Buza, V., et al. 2014, *Monthly Notices of the Royal Astronomical Society*, 445, 1084